

1

²A SEARCH FOR LONG-LIVED, CHARGED, SUPERSYMMETRIC PARTICLES
³USING IONIZATION WITH THE ATLAS DETECTOR

4

BRADLEY AXEN

5

September 2016 – Version 0.25

6



⁸ Bradley Axen: *A Search for Long-Lived, Charged, Supersymmetric Particles using Ion-
⁹ ization with the ATLAS Detector*, Subtitle, © September 2016

¹⁰

Usually a quotation.

¹¹

Dedicated to.

₁₂ ABSTRACT

₁₃ How to write a good abstract:

₁₄ <https://plg.uwaterloo.ca/~migod/research/beck00PSLA.html>

₁₅ PUBLICATIONS

₁₆ Some ideas and figures have appeared previously in the following publications:

₁₇

₁₈ Put your publications from the thesis here. The packages `multibib` or `bibtopic`
₁₉ etc. can be used to handle multiple different bibliographies in your document.

²¹ ACKNOWLEDGEMENTS

²² Put your acknowledgements here.

²³

²⁴ And potentially a second round.

²⁵

26 CONTENTS

27	I	INTRODUCTION	1
28	1	INTRODUCTION	3
29	II	THEORETICAL CONTEXT	5
30	2	STANDARD MODEL	7
31	2.1	Particles	7
32	2.2	Interactions	8
33	2.3	Limitations	8
34	3	SUPERSYMMETRY	9
35	3.1	Motivation	9
36	3.2	Structure	9
37	3.3	Phenomenology	9
38	4	LONG-LIVED PARTICLES	11
39	4.1	Mechanisms	11
40	4.1.1	Examples in Supersymmetry	11
41	4.2	Phenomenology	11
42	4.2.1	Disimilarities to Prompt Decays	11
43	4.2.2	Characteristic Signatures	11
44	III	EXPERIMENTAL STRUCTURE AND RECONSTRUCTION	13
45	5	THE LARGE HADRON COLLIDER	15
46	5.1	Injection Chain	15
47	5.2	Design and Parameters	15
48	5.3	Luminosity	15
49	6	THE ATLAS DETECTOR	17
50	6.1	Coordinate System	17
51	6.2	Magnetic Field	17
52	6.3	Inner Detector	17
53	6.3.1	Pixel Detector	17
54	6.3.2	Semiconductor Tracker	17
55	6.3.3	Transition Radiation Tracker	17
56	6.4	Calorimetry	17
57	6.4.1	Electromagnetic Calorimeters	17
58	6.4.2	Hadronic Calorimeters	17
59	6.4.3	Forward Calorimeters	17
60	6.5	Muon Spectrometer	17
61	6.6	Trigger	17
62	6.6.1	Trigger Scheme	17
63	6.6.2	Missing Transverse Energy Triggers	17
64	7	EVENT RECONSTRUCTION	19
65	7.1	Tracks and Vertices	19

66	7.1.1	Track Reconstruction	19
67	7.1.2	Vertex Reconstruction	19
68	7.2	Jets	19
69	7.2.1	Topological Clustering	19
70	7.2.2	Jet Energy Scale	19
71	7.2.3	Jet Energy Scale Uncertainties	19
72	7.2.4	Jet Energy Resolution	19
73	7.3	Electrons	19
74	7.3.1	Electron Identification	19
75	7.4	Muons	19
76	7.4.1	Muon Identification	19
77	7.5	Missing Transverse Energy	19
78	IV	CALORIMETER RESPONSE	21
79	8	RESPONSE MEASUREMENT WITH SINGLE HADRONS	23
80	8.1	Dataset and Simulation	24
81	8.1.1	Data Samples	24
82	8.1.2	Simulated Samples	24
83	8.1.3	Event Selection	24
84	8.2	Inclusive Hadron Response	25
85	8.2.1	E/p Distribution	26
86	8.2.2	Zero Fraction	26
87	8.2.3	Neutral Background Subtraction	28
88	8.2.4	Corrected Response	28
89	8.3	Identified Particle Response	34
90	8.3.1	Decay Reconstruction	34
91	8.3.2	Identified Response	35
92	8.3.3	Additional Species in Simulation	37
93	8.4	Summary	38
94	9	JET ENERGY RESPONSE AND UNCERTAINTY	41
95	9.1	Motivation	41
96	9.2	Uncertainty Estimate	41
97	9.3	Summary	44
98	V	SEARCH FOR LONG-LIVED PARTICLES	47
99	10	LONG-LIVED PARTICLES IN ATLAS	49
100	10.1	Overview and Characteristics	49
101	10.2	Simulation	49
102	11	EVENT SELECTION	51
103	11.1	Trigger	52
104	11.2	Kinematics and Isolation	52
105	11.3	Standard Model Rejection	55
106	11.4	Ionization	55
107	11.4.1	dE/dx Calibration	55
108	11.4.2	Mass Estimation	55
109	12	BACKGROUND ESTIMATION	57

110	12.1	Background Sources	57
111	12.2	Prediction Method	57
112	12.3	Validation and Uncertainty	57
113	13	SYSTEMATIC UNCERTAINTIES AND RESULTS	59
114	13.1	Systematic Uncertainties	59
115	13.2	Final Yields	59
116	14	INTERPRETATION	61
117	14.1	Cross Sectional Limits	61
118	14.2	Mass Limits	61
119	14.3	Context for Long-Lived Searches	61
120	VI	CONCLUSIONS	63
121	15	SUMMARY AND OUTLOOK	65
122	15.1	Summary	65
123	15.2	Outlook	65
124	VII	APPENDIX	67
125	A	INELASTIC CROSS SECTION	69
126	B	APPENDIX TEST	71
127	B.1	Appendix Section Test	71
128	B.1.1	Appendix Subection Test	71
129	B.2	A Table and Listing	71
130	B.3	Some Formulas	72
131		BIBLIOGRAPHY	75

132 LIST OF FIGURES

133	Figure 1	The particle content of the Standard Model (SM).	8
134	Figure 2	An illustration (a) of the E/p variable used throughout this paper. The red energy deposits come from the charged particle targeted for measurement, while the blue energy deposits are from nearby neutral particles and must be subtracted. The same diagram (b) for the neutral-background selection, described in Section 8.2.3.	25
135			
136			
137			
138			
139			
140	Figure 3	The E/p distribution and ratio of simulation to data for isolated tracks with (a) $ \eta < 0.6$ and $1.2 < p/\text{GeV} < 1.8$ and (b) $ \eta < 0.6$ and $2.2 < p/\text{GeV} < 2.8$	26
141			
142			
143	Figure 4	The fraction of tracks as a function (a, b) of momentum, (c, d) of interaction lengths with $E \leq 0$ for tracks with positive (on the left) and negative (on the right) charge.	27
144			
145			
146			
147	Figure 5	$\langle E/p \rangle_{\text{BG}}$ as a function of the track momentum for tracks with (a) $ \eta < 0.6$, (b) $0.6 < \eta < 1.1$, and as a function of the track pseudorapidity for tracks with (c) $1.2 < p/\text{GeV} < 1.8$, (d) $1.8 < p/\text{GeV} < 2.2$	29
148			
149			
150			
151	Figure 6	$\langle E/p \rangle_{\text{COR}}$ as a function of track momentum, for tracks with (a) $ \eta < 0.6$, (b) $0.6 < \eta < 1.1$, (c) $1.8 < \eta < 1.9$, and (d) $1.9 < \eta < 2.3$	30
152			
153			
154	Figure 7	$\langle E/p \rangle_{\text{COR}}$ calculated using LCW-calibrated topological clusters as a function of track momentum for tracks with (a) zero or more associated topological clusters or (b) one or more associated topological clusters.	31
155			
156			
157			
158	Figure 8	Comparison of the $\langle E/p \rangle_{\text{COR}}$ for tracks with (a) less than and (b) greater than 20 hits in the TRT.	32
159			
160	Figure 9	Comparison of the $\langle E/p \rangle_{\text{COR}}$ for (a) positive and (b) negative tracks as a function of track momentum for tracks with $ \eta < 0.6$	32
161			
162			
163	Figure 10	Comparison of the E/p distributions for (a) positive and (b) negative tracks with $0.8 < p/\text{GeV} < 1.2$ and $ \eta < 0.6$, in simulation with the FTFP_BERT and QGSP_BERT physics lists.	33
164			
165			
166			
167	Figure 11	Comparison of the response of the hadronic calorimeter as a function of track momentum (a) at the EM-scale and (b) after the LCW calibration.	33
168			
169			
170	Figure 12	Comparison of the response of the EM calorimeter as a function of track momentum (a) at the EM-scale and (b) with the LCW calibration.	34
171			
172			

173	Figure 13	The reconstructed mass peaks of (a) K_S^0 , (b) Λ , and (c) $\bar{\Lambda}$ candidates.	35
174			
175	Figure 14	The E/p distribution for isolated (a) π^+ , (b) π^- , (c) proton, and (d) anti-proton tracks.	36
176			
177	Figure 15	The fraction of tracks with $E \leq 0$ for identified (a) π^+ and π^- , and (b) proton and anti-proton tracks	36
178			
179	Figure 16	The difference in $\langle E/p \rangle$ between (a) π^+ and π^- (b) p and π^+ , and (c) \bar{p} and π^-	37
180			
181	Figure 17	$\langle E/p \rangle_{\text{COR}}$ as a function of track momentum for (a) π^+ tracks and (b) π^- tracks.	38
182			
183	Figure 18	The ratio of the calorimeter response to single parti- cles of various species to the calorimeter response to π^+ with the physics list FTFP_BERT.	38
184			
185	Figure 19	The spectra of true particles inside anti- k_t , $R = 0.4$ jets with (a) $90 < p_T/\text{GeV} < 100$, (b) $400 < p_T/\text{GeV} <$ 500 , and (c) $1800 < p_T/\text{GeV} < 2300$	42
186			
187	Figure 20	The jet energy scale (JES) uncertainty contributions, as well as the total JES uncertainty, as a function of jet p_T for (a) $ \eta < 0.6$ and (b) $0.6 < \eta < 1.1$	44
188			
189	Figure 21	The JES correlations as a function of jet p_T and $ \eta $ for jets in the central region of the detector.	45
190			
191	Figure 22	The trigger efficiency of the E_T^{miss} trigger as a function of mass and lifetime.	52
192			
193	Figure 23	The distribution of E_T^{miss} for data and simulated signal events, after the trigger requirement.	53
194			
195	Figure 24	The dependence of dE/dx on N_{split} in data after basic track hit requirements have been applied.	54
196			
197	Figure 25	The distribution of dE/dx with various selections ap- plied in data and simulated signal events.	55
198			
199	Figure 26	The distribution of track momentum for data and sim- ulated signal events, after previous selection require- ments have been applied.	55
200			
201	Figure 27	The distribution of summed tracked momentum within a cone of $\Delta R < 0.2$ around the candidate track for data and simulated signal events, after previous selec- tion requirements have been applied.	56
202			
203	Figure 28	The normalized, two-dimensional distribution of E/p and EM fraction for simulated (a) $Z \rightarrow ee$, (b) $Z \rightarrow \tau\tau$ and (c) 1200 GeV R-Hadron events.	56
204			
205			
206			
207			
208			
209			
210			
211			

₂₁₂ LIST OF TABLES

₂₁₃	Table 1	The dominant sources of corrections and systematic uncertainties in the JES estimation technique, including typical values for the correcting shift (Δ) and the associated uncertainty (σ).	₄₃
₂₁₄			
₂₁₅			
₂₁₆			
₂₁₇	Table 2	Autem usu id	₇₁

218 LISTINGS

<small>219</small> Listing 1	A floating example (<code>listings</code> manual)	72
------------------------------	--	----

220 ACRONYMS

- 221 SM Standard Model
222 LHC Large Hadron Collider
223 ToT time over threshold
224 LCW local cluster weighted
225 MIP minimally ionizing particle
226 EPJC European Physical Journal C
227 JES jet energy scale
228 LLP Long-Lived Particle

229

PART I

230

INTRODUCTION

231

You can put some informational part preamble text here.

1

232

233 INTRODUCTION

234

PART II

235

THEORETICAL CONTEXT

236

You can put some informational part preamble text here.

2

237

238 STANDARD MODEL

239 The SM of particle physics seeks to explain the symmetries and interactions of
240 all currently discovered fundamental particles. It has been tested by several genera-
241 tions of experiments and has been remarkably successful, no significant de-
242 viations have been found. The SM provides predictions in particle physics for
243 interactions up to the Planck scale (10^{15} - 10^{19} GeV).

244 The theory itself is a quantum field theory grown from an underlying $SU(3) \times$
245 $SU(2) \times U(1)$ that requires the particle content and quantum numbers consist-
246 ent with experimental observations (see Section 2.1). Each postulated symme-
247 try is accompanied by an interaction between particles through gauge invari-
248 ance. These interactions are referred to as the Strong, Weak, and Electromag-
249 netic forces, which are discussed in Section 2.2.

250 Although this model has been very predictive, the theory is incomplete; for
251 example, it is not able to describe gravity or astronomically observed dark matter.
252 These limitations are discussed in more detail in Section 2.3.

253 21 PARTICLES

254 The most familiar matter in the universe is made up of protons, neutrons, and
255 electrons. Protons and neutrons are composite particles, however, and are made
256 up in turn by particles called quarks. Quarks carry both electric charge and color
257 charge, and are bound in color-neutral combinations called baryons. The elec-
258 tron is an example of a lepton, and carries only electric charge. Another type
259 of particle, the neutrino, does not form atomic structures in the same way that
260 quarks and leptons do because it carries no color or electric charge. Collectively,
261 these types of particles are known as fermions, the group of particles with half-
262 integer spin.

263 There are three generations of fermions, although familiar matter is formed
264 predominantly by the first generation. The generations are identical except for
265 their masses, which increase in each generation by convention. In addition, each
266 of these particles is accompanied by an antiparticle, with opposite-sign quantum
267 numbers but the same mass.

268 The fermions comprise what is typically considered matter, but there are
269 additional particles that are mediators of interactions between those fermions.
270 These mediators are known as the gauge bosons, gauge in that their existence
271 is required by gauge invariance (discussed further in Section 2.2) and bosons in
272 that they have integer spin. The boson which mediates the electromagnetic force
273 is the photon, the first boson to be discovered; it has no electric charge, no mass,
274 and a spin of 1. There are three spin-1 mediators of the weak force, the two W
275 bosons and the Z boson. The W bosons have electric charge of ± 1 and a mass of
276 80.385 ± 0.015 GeV, while the Z boson is neutral and has a mass of $91.1876 \pm$

277 0.0021 GeV. The strong force is mediated by eight particles called gluons, which
 278 are massless and electrically neutral but do carry color charge.

279 The final particle present in the SM is the Higgs boson, which was recently
 280 observed for the first time by experiments at CERN in 2012. It is electrically
 281 neutral, has a mass of 125.7 ± 0.4 GeV, and is the only spin-0 particle yet to be
 282 observed. The Higgs boson is the gauge boson associated with the mechanism
 283 that gives a mass to the W and Z bosons.

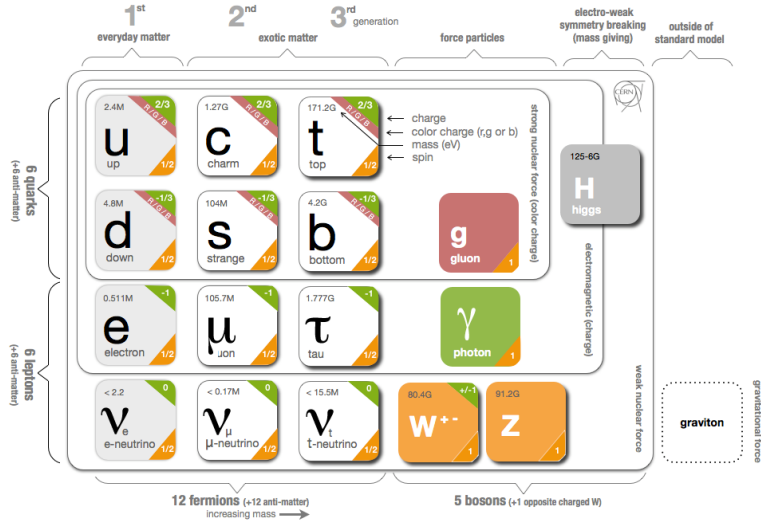


Figure 1: The particle content of the SM.

284 Together these particles form the entire content of the SM, and are summa-
 285 rized in Figure 1. These are the particles that constitute the observable universe
 286 and all the so-far-observed interactions within it.

287 2.2 INTERACTIONS

288 The interactions predicted and described by the SM are fundamentally tied to the
 289 particles within it, both in that they describe the way those particles can influence
 290 each other and also in that the existence of the interactions requires the existence
 291 of some particles (the gauge bosons).

292 2.3 LIMITATIONS

3

293

294 SUPERSYMMETRY

295 3.1 MOTIVATION

296 3.2 STRUCTURE

297 3.3 PHENOMENOLOGY

4

298

299 LONG-LIVED PARTICLES

300 4.1 MECHANISMS

301 4.1.1 EXAMPLES IN SUPERSYMMETRY

302 4.2 PHENOMENOLOGY

303 4.2.1 DISIMILARITIES TO PROMPT DECAYS

304 4.2.2 CHARACTERISTIC SIGNATURES

305

PART III

306

EXPERIMENTAL STRUCTURE AND RECONSTRUCTION

307

You can put some informational part preamble text here.

5

308

309 THE LARGE HADRON COLLIDER

310 5.1 INJECTION CHAIN

311 5.2 DESIGN AND PARAMETERS

312 5.3 LUMINOSITY

6

313

314 THE ATLAS DETECTOR

315 6.1 COORDINATE SYSTEM

316 6.2 MAGNETIC FIELD

317 6.3 INNER DETECTOR

318 6.3.1 PIXEL DETECTOR

319 6.3.2 SEMICONDUCTOR TRACKER

320 6.3.3 TRANSITION RADIATION TRACKER

321 6.4 CALORIMETRY

322 6.4.1 ELECTROMAGNETIC CALORIMETERS

323 6.4.2 HADRONIC CALORIMETERS

324 6.4.3 FORWARD CALORIMETERS

325 6.5 MUON SPECTROMETER

326 6.6 TRIGGER

327 6.6.1 TRIGGER SCHEME

328 6.6.2 MISSING TRANSVERSE ENERGY TRIGGERS

7

329

330 EVENT RECONSTRUCTION

331 The ATLAS experiment combines measurements in the subdetectors to form a
332 cohesive picture of each physics event.

333 7.1 TRACKS AND VERTICES

334 7.1.1 TRACK RECONSTRUCTION

335 7.1.1.1 NEURAL NETWORK

336 7.1.1.2 PIXEL DE/DX

337 7.1.2 VERTEX RECONSTRUCTION

338 7.2 JETS

339 7.2.1 TOPOLOGICAL CLUSTERING

340 7.2.2 JET ENERGY SCALE

341 7.2.3 JET ENERGY SCALE UNCERTAINTIES

342 7.2.4 JET ENERGY RESOLUTION

343 7.3 ELECTRONS

344 7.3.1 ELECTRON IDENTIFICATION

345 7.4 MUONS

346 7.4.1 MUON IDENTIFICATION

347 7.5 MISSING TRANSVERSE ENERGY

348

PART IV

349

CALORIMETER RESPONSE

350

You can put some informational part preamble text here.

8

351

352 RESPONSE MEASUREMENT WITH SINGLE HADRONS

353 As discussed in Section 7.2, colored particles produced in collisions hadronize
354 into jets of multiple hadrons. One approach to understanding jet physics in the
355 ATLAS calorimetry is to evaluate the calorimeter response to those individual
356 hadrons; measurements of individual hadrons can be used to build up an under-
357 standing of the jets that they form. The redundancy of the momentum provided
358 by the tracking system and the energy provided by the calorimeter provides an
359 opportunity to study calorimeter response using real collisions, as described fur-
360 ther in Section 8.2.

361 Calorimeter response includes a number of physical effects that can be ex-
362 tracted to provide insight into many aspects of jet modeling. First, many charged
363 hadrons interact with the material of the detector prior to reaching the calorime-
364 ters and thus do not deposit any energy. Comparing this effect in data and sim-
365 ulation is a powerful tool in validating the interactions of particles with the ma-
366 terial of the detector and the model of the detector geometry in simulation, see
367 Section 8.2.2. The particles which do reach the calorimeter deposit their energy
368 into individual cells, which are then clustered to measure full energy deposits.
369 Comparing the response in data to simulated hadrons provides a direct evalua-
370 tion of noise in the calorimeters, the showering of hadronic particles, and the
371 energy deposited by particles in matter (Section 8.2.4). These measurements are
372 extended to explore several additional effects, such as the dependence on charge,
373 in Section 8.2.4.1.

374 The above studies all use an inclusive selection of charged particles, which are
375 comprised predominantly of pions, kaons, and (anti)protons. It is also possible
376 to measure the particle types separately to evaluate the simulated interactions of
377 each particle, particularly at low energies where differences between species are
378 very relevant. Pions and (anti)protons can be identified through decays of long-
379 lived particles, in particular Λ , $\bar{\Lambda}$, and K_S^0 , and then used to measure response as
380 described above. This is discussed in detail in Section 8.3.

381 Together, these measurements in data provide a thorough understanding of
382 the way hadrons interact with the ATLAS detector and can be used to build up a
383 description of jets, as seen in Chapter 9. The results in this chapter use data col-
384 lected at 7 and 8 TeV collected in 2010 and 2012, respectively. Both are included
385 as the calorimeter was repaired and recalibrated between those two data-taking
386 periods. Both sets of data are compared to an updated simulation that includes
387 new physics models provided by Geant4 [12] and improvements in the detec-
388 tor description [2, 6]. These results are published in European Physical Journal
389 C (EPJC) [8] and can be compared to a similar measurement performed in 2009
390 and 2010 [5], which used the previous version of the simulation framework [1].

391 8.1 DATASET AND SIMULATION

392 8.1.1 DATA SAMPLES

393 The two datasets used in this chapter are taken from dedicated low-pileup runs
 394 where the fraction of events with multiple interactions was negligible, to facilitate
 395 measurement of isolated hadrons. The 2012 dataset at $\sqrt{s} = 8$ TeV contains
 396 8 million events and corresponds to an integrated luminosity of 0.1 nb^{-1} . The
 397 2010 dataset at $\sqrt{s} = 7$ TeV contains 3 million events and corresponds to an
 398 integrated luminosity of 3.2 nb^{-1} . The latter dataset was also used in the 2010
 399 results [5], but it has since been reanalyzed with an updated detector description
 400 for the material and alignment.

401 8.1.2 SIMULATED SAMPLES

402 The two datasets above are compared to simulated single-, double-, and non-
 403 diffractive events generated with Pythia8 [32] using the A2 configuration of
 404 hadronization [3] and the MSTW 2008 parton-distribution function set [28, 31].
 405 The conditions and energies for each run are matched in the two simulations.

406 To evaluate the interaction of hadrons with detector material, the simulation
 407 uses two different collections of hadronic physics models, called physics lists, in
 408 Geant4 9.4 [30]. The first, QGSP_BERT, combines the Bertini intra-nuclear
 409 cascade [17, 24, 26] below 9.9 GeV, a parametrized proton inelastic model from
 410 9.5 to 25 GeV [21], and a quark-gluon string model above 12 GeV [13, 14, 18, 19,
 411 22]. The second, FTFP_BERT, combines the Bertini intra-nuclear cascade [17, 24,
 412 26] below 5 GeV and the Fritiof model [15, 16, 23, 29] above 4 GeV. In either list,
 413 Geant4 enforces a smooth transition between models where multiple models
 414 overlap.

415 8.1.3 EVENT SELECTION

416 The event selection for this study is minimal, as the only requirement is selecting
 417 good-quality events with an isolated track. Such events are triggered by requiring
 418 at least two hits in the minimum-bias trigger scintillators. After trigger, each
 419 event is required to have exactly one reconstructed vertex, and that vertex is re-
 420 quired to have four or more associated tracks.

421 The particles which enter into the response measurements are first identified
 422 as tracks in the inner detector. The tracks are required to have at least 500 MeV
 423 of transverse momentum. To ensure a reliable momentum measurement, these
 424 tracks are required to have at least one hit in the pixel detector, six hits in the SCT,
 425 and small longitudinal and transverse impact parameters with respect to the pri-
 426 mary vertex [5]. For the majority of the measurements in this chapter, the track is
 427 additionally required to have 20 hits in the TRT, which significantly reduces the
 428 contribution from tracks which undergo nuclear interactions. This requirement
 429 and its effect is discussed in more detail in Section 8.2.4.1. In addition, tracks are
 430 rejected if there is another track which extrapolates to the calorimeter within a

431 cone of $\Delta R = \sqrt{(\Delta\phi)^2 + (\Delta\eta)^2} < 0.4$. This requirement guarantees that the
432 contamination of energy from nearby charged particles is negligible [5].

433 8.2 INCLUSIVE HADRON RESPONSE

434 The calorimeter response is more precisely defined as the ratio of the measured
435 calorimeter energy to the true energy carried by the particle, although this true
436 energy is unknown. For charged particles, however, the inner detector provides
437 a very precise measurement of momentum (with uncertainty less than 1%) that
438 can be used as a proxy for true energy. The ratio of the energy deposited by the
439 charged particle in the calorimeter, E , to its momentum measured in the inner
440 detector p , forms the calorimeter response measure called E/p . Though the dis-
441 tribution of E/p contains a number of physical features, this study focuses on
442 the trends in two aggregated quantities: $\langle E/p \rangle$, the average of E/p within a given
443 subset of particles, and the zero fraction, the fraction of particles with no associ-
444 ated energy in the calorimeter.

445 The calorimeter energy assigned to a track particle is defined using clusters.
446 The clusters are formed using a 4–2–0 algorithm [9] that begins with seeds re-
447quiring at least 4 times the average calorimeter noise. The neighboring cells with
448 at least twice that noise threshold are then added to the cluster, and all bound-
449ing cells are then added with no requirement. This algorithm minimizes noise
450 contributions through its seeding process, and including the additional layers
451 improves the energy resolution [33]. The clusters are associated to a given track
452 if they fall within a cone of $\Delta R = 0.2$ of the extrapolated position of the track,
453 which includes about 90% of the energy on average [5]. This construction is il-
454lustrated in Figure 2.

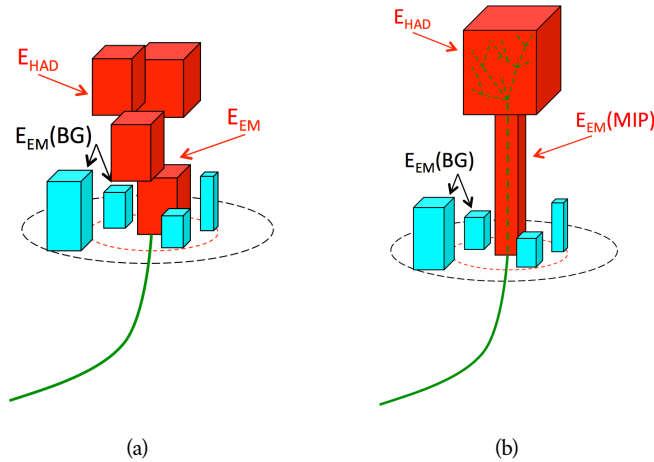
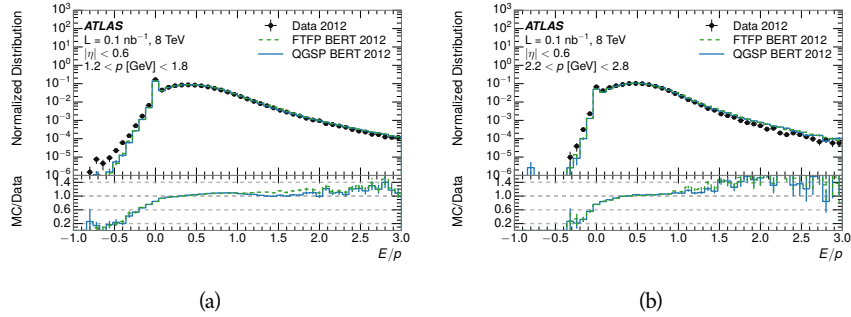


Figure 2: An illustration (a) of the E/p variable used throughout this paper. The red energy deposits come from the charged particle targeted for measurement, while the blue energy deposits are from nearby neutral particles and must be subtracted. The same diagram (b) for the neutral-background selection, described in Section 8.2.3.

455 8.2.1 E/P DISTRIBUTION

456 The E/p distributions measured in both data and simulation are shown in Figure 3 for two example bins of track momentum and for tracks in the central
 457 region of the detector. These distributions show several important features of
 458 the E/p observable. The large content in the bin at $E = 0$ comes from tracks that
 459 have no associated cluster, which occurs due to interactions with detector mate-
 460 rial prior to reaching the calorimeter or the energy deposit being insufficiently
 461 large to generate a seed, and are discussed in Section 8.2.2. The small negative
 462 tail comes from similar tracks that do not deposit any energy in the calorime-
 463 ter but are randomly associated to a noise cluster. The long positive tail above
 464 1.0 comes from the contribution of neutral particles. Nearby neutral particles
 465 deposit (sometimes large) additional energy in the calorimeter but do not pro-
 466 duce tracks in the inner detector, so they cannot be rejected by the track isol-
 467 ation requirement. Additionally the peak and mean of the distribution falls below
 468 1.0 because of the loss of energy not found within the cone as well as the non-
 469 compensation of the calorimeter.
 470

471 The data and simulation share the same features, but the high and low tails
 472 are significantly different. The simulated events tend to overestimate the contri-
 473 bution of neutral particles to the long tail, an effect which can be isolated and
 474 removed as discussed in Section 8.2.3. Additionally, the simulated clusters have
 475 less noise on average, although this is a small effect on the overall response.



476 Figure 3: The E/p distribution and ratio of simulation to data for isolated tracks with
 477 (a) $|\eta| < 0.6$ and $1.2 < p/\text{GeV} < 1.8$ and (b) $|\eta| < 0.6$ and $2.2 < p/\text{GeV} < 2.8$.

476 8.2.2 ZERO FRACTION

477 The fraction of particles with no associated clusters, or similarly those with $E \leq$
 478 0, reflects the modeling of both the detector geometry and hadronic interactions.
 479 The zero fraction is expected to rise as the amount of material a particle traverses
 480 increases, while it is expected to decrease as the particle energy increases. This
 481 dependence can be seen in Figure 4, where the zero fraction in data and simula-
 482 tion is shown as a function of momentum and the amount of material measured
 483 in interaction lengths. The trends are similar between the 2010 and 2012 mea-
 484 surements. The zero fraction decreases with energy as expected. The amount of

material in the detector increases with η , which provides a distribution of interaction lengths. As the data and simulation have significant disagreement in the zero fraction over a number of interaction lengths, the difference must be primarily from the modeling of hadronic interactions with detector material and not just the detector geometry.

There is also a noticeable difference between positive and negative tracks at low momentum, which reflects the difference in response between protons and antiprotons. Antiprotons have significant model differences in the two physics lists, QGSP_BERT and FTFP_BERT, and this is evident in the lowest momentum bin of the data to simulation ratio. This difference is explored further in Section 8.3.

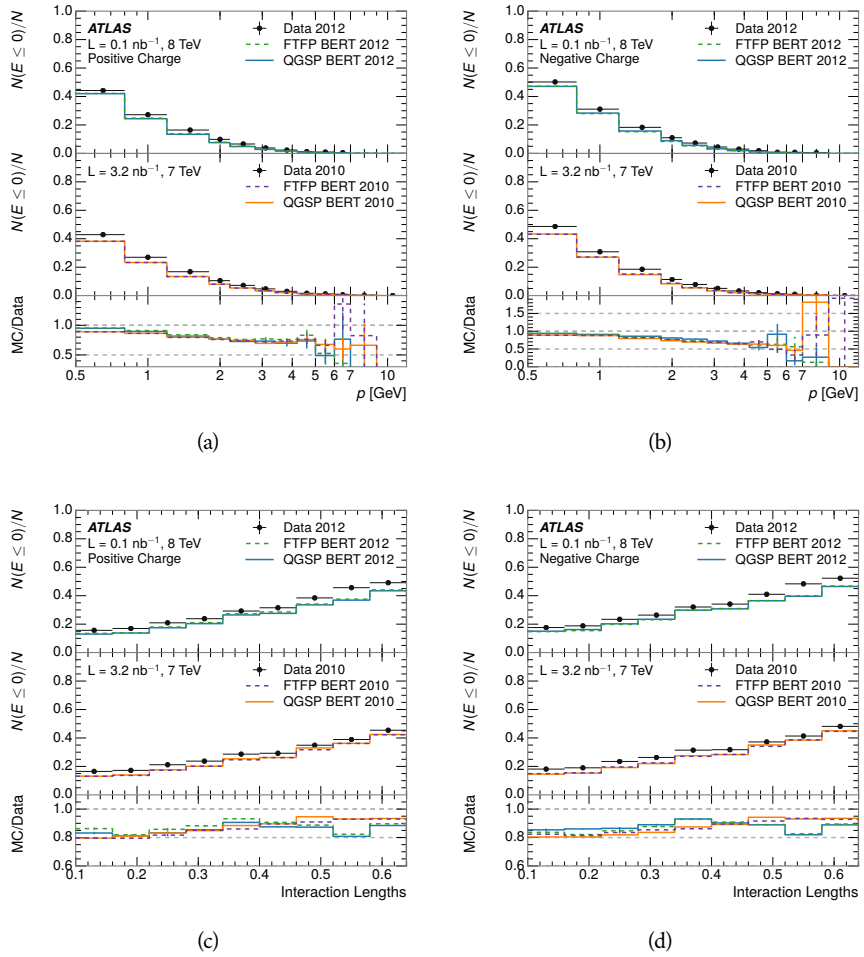


Figure 4: The fraction of tracks as a function (a, b) of momentum, (c, d) of interaction lengths with $E \leq 0$ for tracks with positive (on the left) and negative (on the right) charge.

496 8.2.3 NEUTRAL BACKGROUND SUBTRACTION

497 The isolation requirement on hadrons is only effective in remove energy contri-
 498 bution from nearby charged particles. Nearby neutral particles, predominantly
 499 photons from π^0 decays, also add their energy to the calorimeter clusters, but
 500 mostly in the electromagnetic calorimeter. It is possible to measure this contri-
 501 bution, on average, using late-showering hadrons that minimally ionize in the
 502 electromagnetic calorimeter. Such particles are selected by requiring that they
 503 deposit less than 1.1 GeV in the EM calorimeter within a cone of $\Delta R < 0.1$
 504 around the track. To ensure that these particles are well measured, they are addi-
 505 tionally required to deposit between 40% and 90% of their energy in the hadronic
 506 calorimeter within the same cone.

507 These particles provide a clean sample to measure the nearby neutral back-
 508 ground because they do not deposit energy in the area immediately surrounding
 509 them in the EM calorimeter, as shown in Figure 2. So, the energy deposits in the
 510 region $0.1 < \Delta R < 0.2$ can be attributed to neutral particles alone. To estimate
 511 the contribution to the whole cone considered for the response measurement,
 512 that energy is scaled by a geometric factor of 4/3. This quantity, $\langle E/p \rangle_{\text{BG}}$, mea-
 513 sured in aggregate over a number of particles, gives the contribution to $\langle E/p \rangle$
 514 from neutral particles in the EM calorimeter. Similar techniques were used in
 515 the individual layers of the hadronic calorimeters to show that the background
 516 from neutrals is negligible in those layers [5].

517 The distribution of this background estimate is shown in Figure 5. Although
 518 the simulation captures the overall trend, it significantly overestimates the neu-
 519 tral contribution for tracks with momentum between 2 and 8 GeV. This effect
 520 was also seen in the tails of the E/p distributions in Figure 3. This difference is
 521 likely due to the modeling of coherent neutral particle radiation in Pythia8, as
 522 the discrepancy does not depend on η and thus is unlikely to be a mismodeling
 523 of the detector. This difference can be subtracted to form a corrected average
 524 E/p , as in Section 8.2.4.

525 8.2.4 CORRECTED RESPONSE

526 Figure 6 shows $\langle E/p \rangle_{\text{COR}}$ as a function of momentum for several bins of pseu-
 527 dorapidity. This corrected $\langle E/p \rangle_{\text{COR}} \equiv \langle E/p \rangle - \langle E/p \rangle_{\text{BG}}$ measures the average
 528 calorimeter response without the contamination of neutral particles. It is the
 529 most direct measurement of calorimeter response in that it is the energy mea-
 530 sured for fully isolated hadrons. The correction is performed separately in data
 531 and simulation, so that the mismodeling of the neutral background in simulation
 532 is removed from the comparison of response. The simulation overestimates the
 533 response at low momentum by about 5%, an effect that can be mostly attributed
 534 to the underestimation of the zero fraction mentioned previously.

535 The response measurement above used topological clustering at the EM scale,
 536 that is clusters were formed to measure energy but no corrections were applied
 537 to correct for expected effects like energy lost outside of the cluster or in unin-
 538 strumented material. It is also interesting to measure $\langle E/p \rangle_{\text{COR}}$ using local clus-

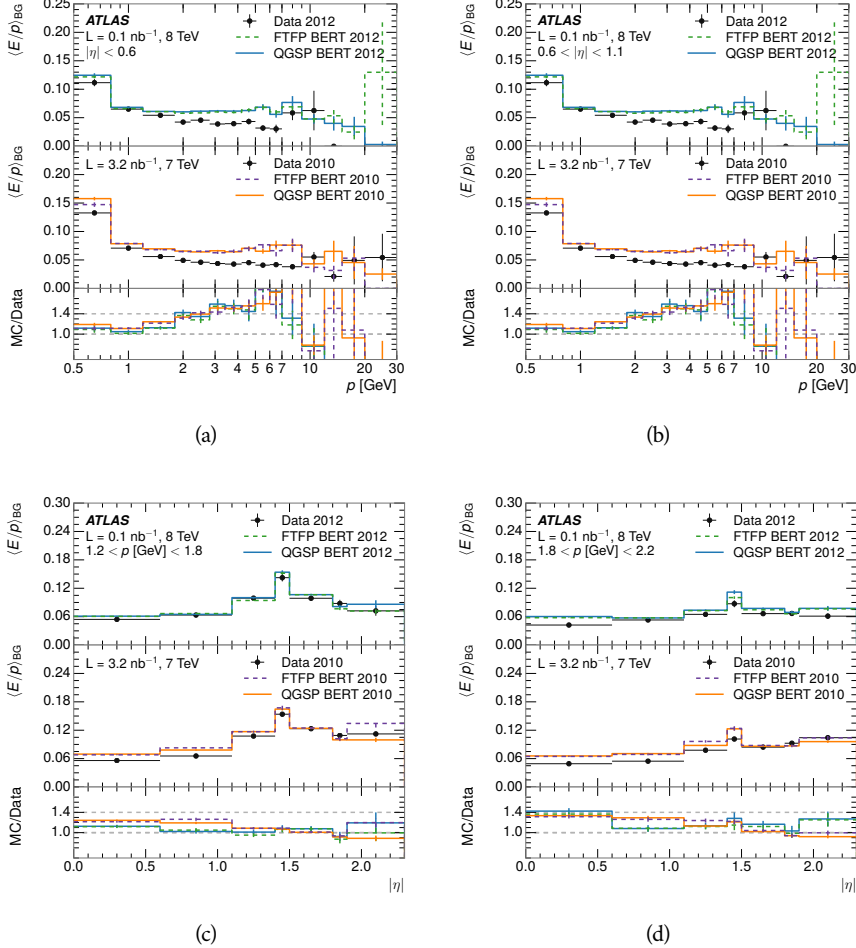


Figure 5: $\langle E/p \rangle_{BG}$ as a function of the track momentum for tracks with (a) $|\eta| < 0.6$, (b) $0.6 < |\eta| < 1.1$, and as a function of the track pseudorapidity for tracks with (c) $1.2 < p/\text{GeV} < 1.8$, (d) $1.8 < p/\text{GeV} < 2.2$.

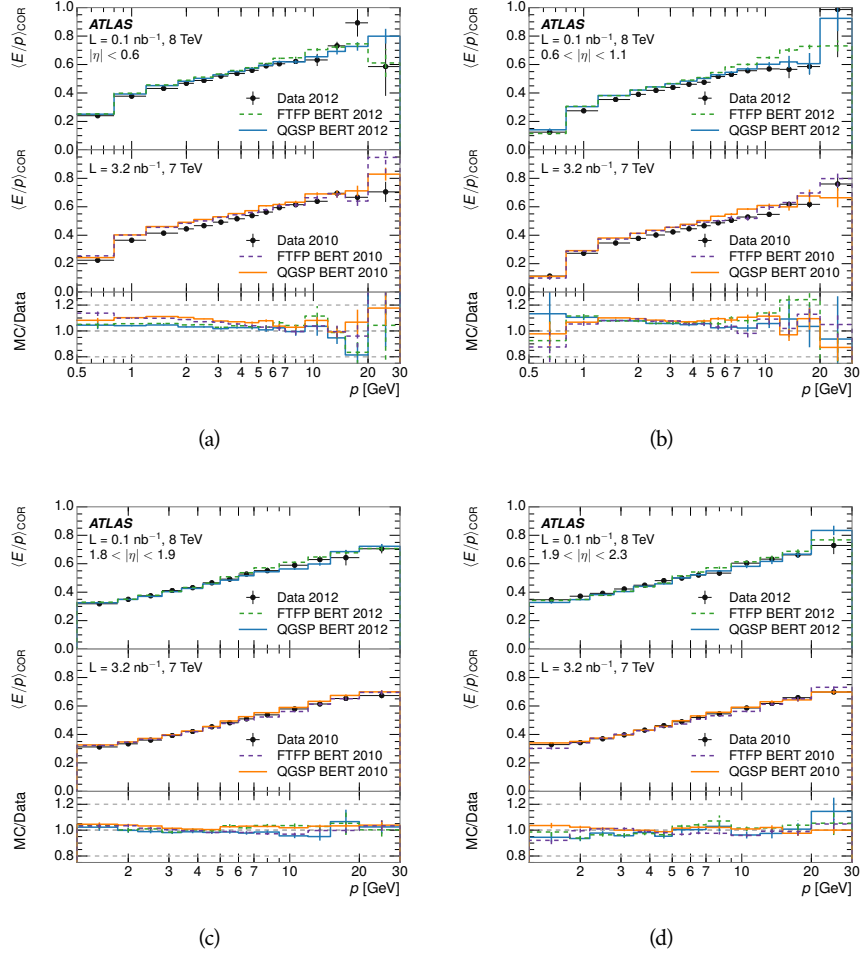


Figure 6: $\langle E/p \rangle_{\text{COR}}$ as a function of track momentum, for tracks with (a) $|\eta| < 0.6$, (b) $0.6 < |\eta| < 1.1$, (c) $1.8 < |\eta| < 1.9$, and (d) $1.9 < |\eta| < 2.3$.

539 ter weighted (LCW) energies, which accounts for those effects by calibrating the
 540 energy based on the properties of the cluster such as energy density and depth
 541 in the calorimeter. Figure 7 shows these distributions for tracks with zero or
 542 more clusters and separately for tracks with one or more clusters. The calibra-
 543 tion moves $\langle E/p \rangle_{\text{COR}}$ significantly closer to 1.0, which is the purpose of the cali-
 544 bration. The agreement between data and simulation improves noticeably when
 545 at least one cluster is required, as this removes the contribution from the mis-
 546 modeling of the zero fraction.

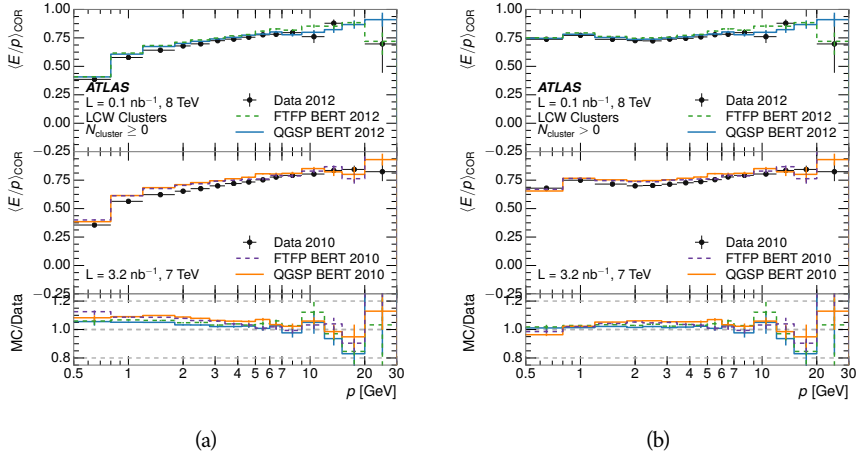


Figure 7: $\langle E/p \rangle_{\text{COR}}$ calculated using LCW-calibrated topological clusters as a function of track momentum for tracks with (a) zero or more associated topological clusters or (b) one or more associated topological clusters.

547 8.2.4.1 ADDITIONAL STUDIES

548 As has been seen in several previous measurements, the simulation does not
 549 correctly model the chance of a low momentum hadron to reach the calorime-
 550 ter. Because of the consistent discrepancy across pseudorapidity and interaction
 551 lengths, this seems to be best explained by incomplete understanding of hadronic
 552 interactions with the detector. For example, a hadron that scatters off of a nu-
 553 cleus in the inner detector can be deflected through a significant angle and not
 554 reach the expected location in the calorimeter. In addition, these interactions can
 555 produce secondary particles that are difficult to model.

556 The requirement on the number of hits in the TRT reduces these effects by
 557 preferentially selecting tracks that do not undergo nuclear interactions. It is in-
 558 teresting to check how well the simulation models tracks with low numbers of
 559 TRT hits, where the nuclear interactions are much more likely. Figure 8 com-
 560 pares the distributions with $N_{\text{TRT}} < 20$ to $N_{\text{TRT}} > 20$ for real and simulated
 561 particles. As expected, the tracks with fewer hits are poorly modeled in the sim-
 562 ulation as $\langle E/p \rangle_{\text{COR}}$ differs by as much as 25% at low momentum.

563 Another interesting aspect of the simulation is the description of antiprotons
 564 at low momentum, where QGSP_BERT and FTFP_BERT have significant differ-
 565 ences. This can be seen to have an effect in the inclusive response measurement

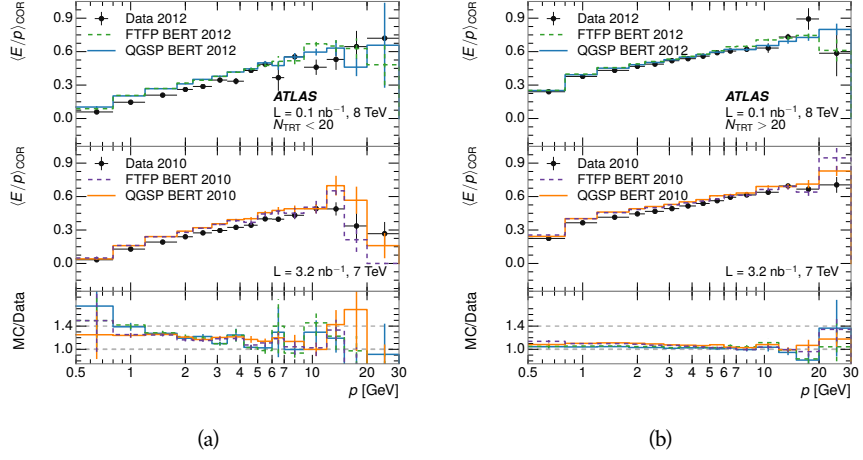


Figure 8: Comparison of the $\langle E/p \rangle_{\text{COR}}$ for tracks with (a) less than and (b) greater than 20 hits in the TRT.

when separated into positive and negative charge. The $\langle E/p \rangle_{\text{COR}}$ distributions for positive and negative particles are shown in Figure 9, where a small difference between QGSP_BERT and FTFP_BERT can be seen in the distribution for negative tracks. This is demonstrated more clearly in Figure 10, which shows the E/p distribution in the two simulations separated by charge. There is a clear difference around $E/p > 1.0$, which can be explained by the additional energy deposited by the annihilation of the antiproton in the calorimeter that is modeled well only in FTFP_BERT. This is also explored with data using identified antiprotons in Section 8.3.

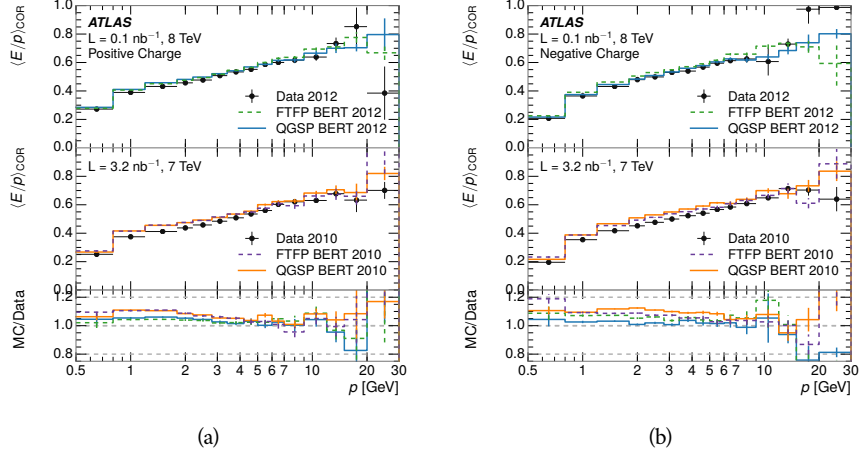


Figure 9: Comparison of the $\langle E/p \rangle_{\text{COR}}$ for (a) positive and (b) negative tracks as a function of track momentum for tracks with $|\eta| < 0.6$.

The $\langle E/p \rangle$ results in previous sections have considered the electromagnetic and hadronic calorimeters together as a single energy measurement, to emphasize the total energy deposited for a given particle. However, the deposits in each

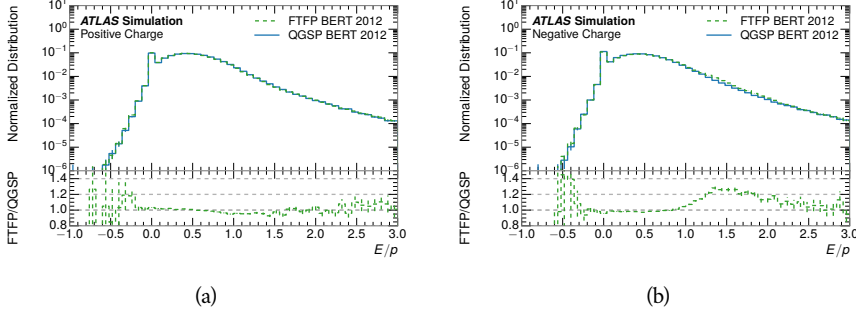


Figure 10: Comparison of the E/p distributions for (a) positive and (b) negative tracks with $0.8 < p/\text{GeV} < 1.2$ and $|\eta| < 0.6$, in simulation with the FTFP_BERT and QGSP_BERT physics lists.

578 calorimeter are available separately and $\langle E/p \rangle$ can be constructed for each layer.
 579 As the layers are composed of different materials and are modeled separately in
 580 the detector geometry, confirmation that the simulation matches the data well
 581 in each layer adds confidence in both the description of hadronic interactions
 582 with the two different materials and also the geometric description of each.

583 The technique discussed in Section 8.2.3 for selecting minimally ionizing par-
 584 ticle (**MIP**)s in the electromagnetic calorimeter is also useful in studying deposits
 585 in the hadronic calorimeter. Those **MIP**s deposit almost all of their energy ex-
 586clusively in the hadronic calorimeter. Figure 11 shows $\langle E/p \rangle_{\text{RAW}}^{\text{Had}}$, where RAW
 587 indicates that no correction has been applied for neutral backgrounds and Had
 588 indicates that only clusters for the hadronic calorimeter are included. The RAW
 589 and COR versions of $\langle E/p \rangle$ in this case are the same, as the neutral background
 590 is negligible in that calorimeter layer. The distributions are shown both for the
 591 original EM scale calibration and after LCW calibration. The data and simulation
 592 agree very well in this comparison, except in the lowest momentum bin which
 593 has 5% discrepancy that has already been seen in similar measurements.

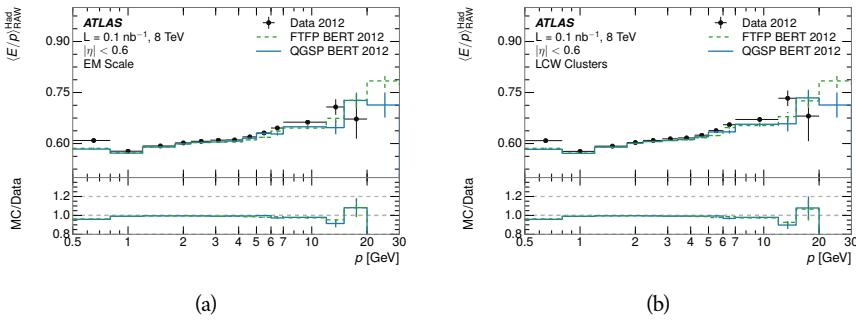


Figure 11: Comparison of the response of the hadronic calorimeter as a function of track momentum (a) at the EM-scale and (b) after the LCW calibration.

594 A similar comparison can be made in the electromagnetic calorimeter by se-
 595 lecting particles which have no associated energy in the hadronic calorimeter.
 596 These results are measured in terms of $\langle E/p \rangle_{\text{COR}}^{\text{EM}}$, where EM designates that

597 only clusters in the electromagnetic calorimeter are included and COR designates
 598 that the neutral background is subtracted as the neutral background is
 599 present in this case. Figure 12 shows the analogous comparisons to Figure 11 in
 600 the electromagnetic calorimeter. In this case the disagreement between data and
 601 simulation is more pronounced, with discrepancies as high as 5% over a larger
 602 range of momenta. This level of discrepancy indicates that the description of the
 603 electromagnetic calorimeter is actually the dominant source of discrepancy in
 604 the combined distributions in Section 8.2.4.

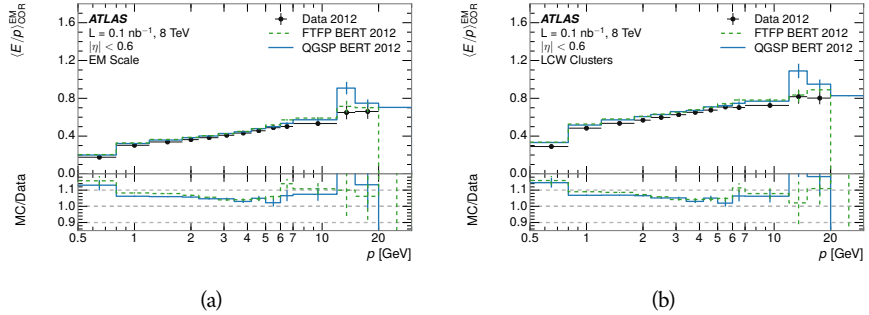


Figure 12: Comparison of the response of the EM calorimeter as a function of track momentum (a) at the EM-scale and (b) with the LCW calibration.

605 **NOTE: There are more studies that I skipped for brevity that could be
 606 included if interesting. E/p at different cluster threshold settings, E/p with
 607 pileup, E/p with cells. I also left out a lot of eta bins that appear in the paper
 608 so that this section didn't turn into 20 pages of plots.**

609 8.3 IDENTIFIED PARTICLE RESPONSE

610 The inclusive response measurement for hadrons can be augmented by measur-
 611 ing the response for specific particle species. The simulation models each parti-
 612 cle type separately, and understanding the properties of each is important in con-
 613 straining the uncertainty on jets. In order to select and measure specific hadrons,
 614 this section relies on the displaced decays of long-lived particles. Such decays can
 615 be identified by reconstructing secondary vertices with a requirement on mass.
 616 In particular, Λ , $\bar{\Lambda}$, and K_S^0 can be used to select a pure sample of protons, an-
 617 tiprotons, and pions, respectively.

618 8.3.1 DECAY RECONSTRUCTION

619 The measurement of response for identified particles uses the same selection
 620 as for inclusive particles (Section 8.1.3) with a few additions. Each event used
 621 is required to have at least one secondary vertex, and the tracks are required
 622 to match to that vertex rather than the primary vertex. Pions are selected from
 623 decays of $K_S^0 \rightarrow \pi^+ \pi^-$, which is the dominant decay for K_S^0 to charged particles.
 624 Protons are selected from decays of $\Lambda \rightarrow \pi^- p$ and antiprotons from $\bar{\Lambda} \rightarrow \pi^+ \bar{p}$,

which are similarly the dominant decays of Λ and $\bar{\Lambda}$ to charged particles. The species of parent hadron in these decays is determined by reconstructing the mass of the tracks associated to the secondary vertex. The sign of the higher momentum decay particle can distinguish between Λ and $\bar{\Lambda}$, which of course have the same mass, as the proton or antiproton is kinematically favored to have higher momentum. Examples of the reconstructed masses used to select these decays are shown in Figure 13.

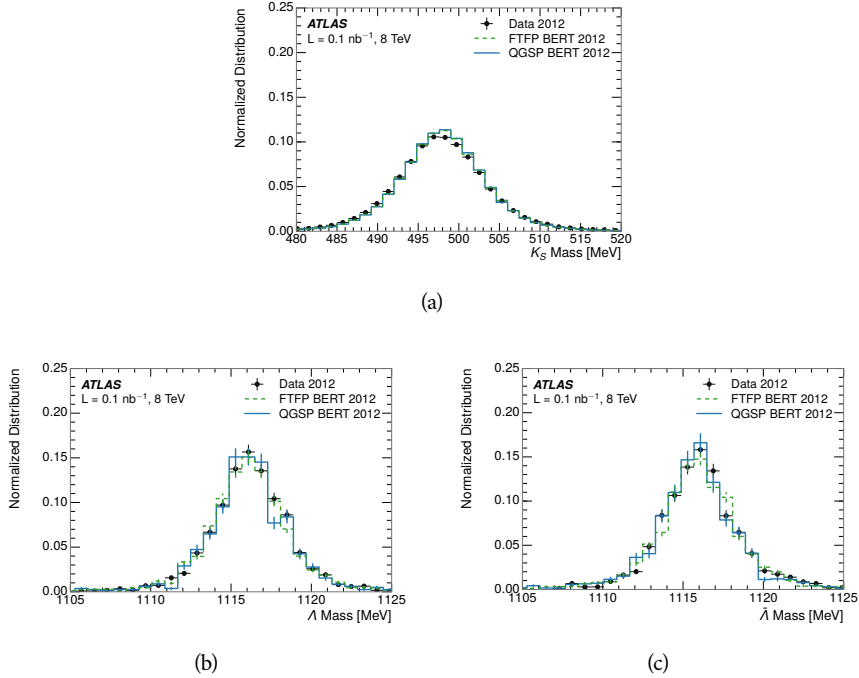


Figure 13: The reconstructed mass peaks of (a) K_S^0 , (b) Λ , and (c) $\bar{\Lambda}$ candidates.

The dominant backgrounds for the identified particle decays are nuclear interactions and combinatoric sources. These are suppressed by the kinematic requirements on the tracks as well as an additional veto which removes candidates that are consistent with both a Λ or $\bar{\Lambda}$ and a K_S^0 hypothesis, which is possible because of the different assumptions on particle mass in each case [5]. After these requirements, the backgrounds are found to be negligible compared to the statistical errors on these measurements.

8.3.2 IDENTIFIED RESPONSE

With these techniques the E/p distributions are extracted in data and simulation for each particle species and shown in Figure 14. These distributions are shown for a particular bin of E_a ($2.2 < E_a/\text{GeV} < 2.8$), rather than p . E_a is the energy available to be deposited in the calorimeter: for pions $E_a = \sqrt{p^2 + m^2}$, for protons $E_a = \sqrt{p^2 + m^2} - m$, and for antiprotons $E_a = \sqrt{p^2 + m^2} + m$. The features of the E/p distributions are similar to the inclusive case. There is a small negative tail from noise and a large fraction of tracks with zero energy from particles which do not reach the calorimeter. The long positive tail is noticeably more

648 pronounced for antiprotons because of the additional energy generated by the
 649 annihilation in addition to the neutral background.

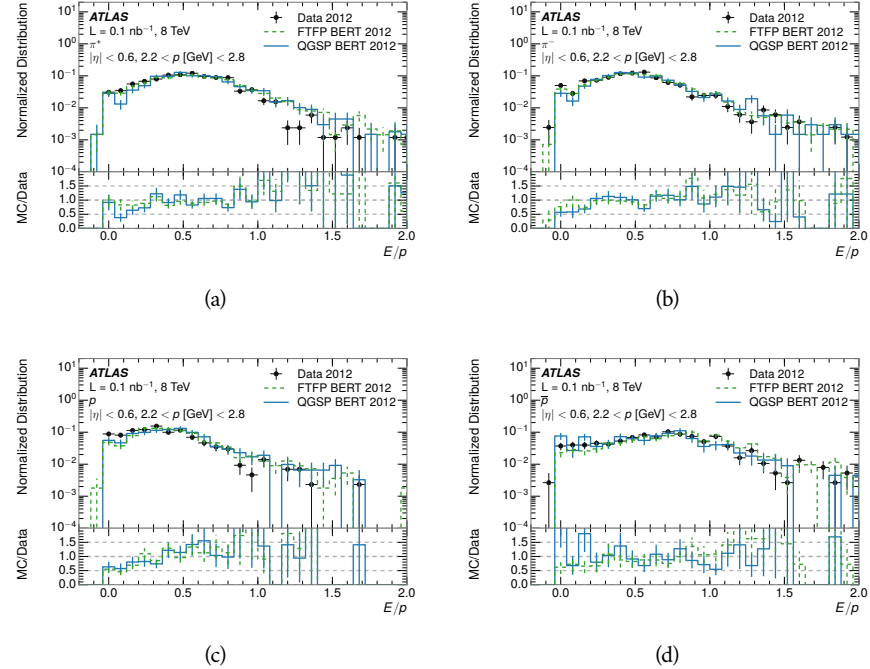


Figure 14: The E/p distribution for isolated (a) π^+ , (b) π^- , (c) proton, and (d) anti-proton tracks.

650 The zero fraction is further explored in Figure 15 for pions and protons in
 651 data and simulation. The simulation consistently underestimates the zero frac-
 652 tion independent of particle species, which implies that this discrepancy is not
 653 caused by the model of a particular species but rather a feature common to all.

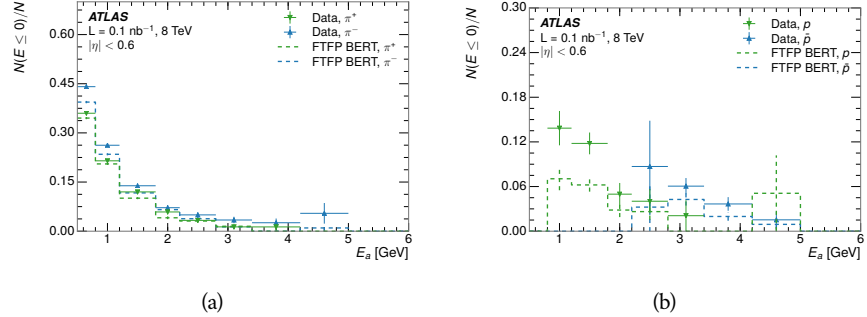


Figure 15: The fraction of tracks with $E \leq 0$ for identified (a) π^+ and π^- , and (b) proton and anti-proton tracks

654 It is also interesting to compare the response between the different particle
 655 species. One approach to do this is to measure the difference in $\langle E/p \rangle$ between
 656 two types, which has the advantage of removing the neutral background. These
 657 differences are shown in various combinations in Figure 16. The response for

658 π^+ is greater on average than the response to π^- because of a charge-exchange
 659 effect which causes the production of additional neutral pions in the showers of
 660 π^+ [20]. The response for π^+ is also greater on average than the response to p ,
 661 because a large fraction of the energy of π^+ hadrons is converted to an electro-
 662 magnetic shower [11, 25]. However, the \bar{p} response is significantly higher than
 663 the response to π^- because of the annihilation of the antiproton. FTFP_BERT
 664 does a better job of modeling this effect than QGSP_BERT because of their differ-
 665 ent descriptions of \bar{p} interactions with material.

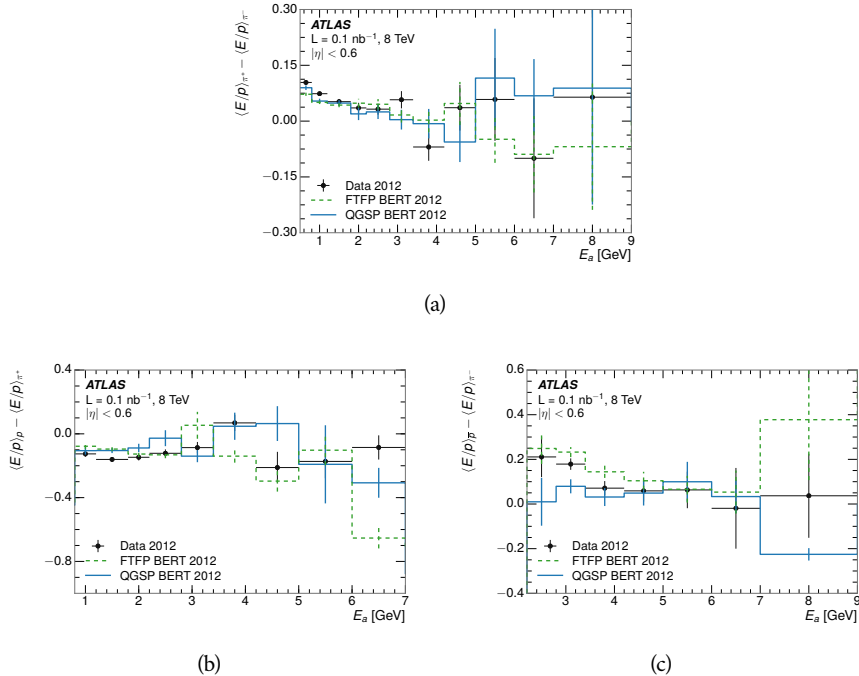


Figure 16: The difference in $\langle E/p \rangle$ between (a) π^+ and π^- (b) p and π^+ , and (c) \bar{p} and π^- .

666 It is also possible to remove the neutral background from these response dis-
 667 tributions using the same technique as in Section 8.2.3. The technique is largely
 668 independent of the particle species and so can be directly applied to $\langle E/p \rangle$ for
 669 pions. The $\langle E/p \rangle_{\text{COR}}$ distributions for pions are shown in Figure 17, which are
 670 very similar to the inclusive results. The inclusive hadrons are comprised mostly
 671 of pions, so this similarity is not surprising. It is also possible to see the small
 672 differences between π^+ and π^- response here, where $\langle E/p \rangle_{\text{COR}}$ is higher on av-
 673 erage for π^+ . The agreement between data and simulation is significantly worse
 674 for the π^- distributions than for the π^+ , with a discrepancy greater than 10%
 675 below 2-3 GeV.

676 8.3.3 ADDITIONAL SPECIES IN SIMULATION

677 The techniques above provide a method to measure the response separately for
 678 only pions and protons. However the hadrons which forms jets include a num-
 679 ber of additional species such as kaons and neutrons. The charged kaons are

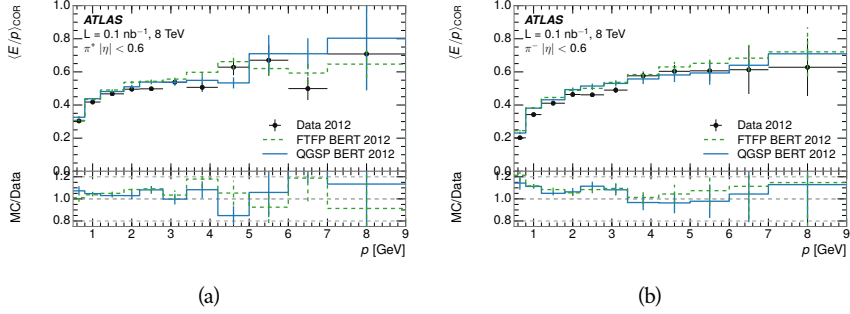


Figure 17: $\langle E/p \rangle_{\text{COR}}$ as a function of track momentum for (a) π^+ tracks and (b) π^- tracks.

680 an important component of the inclusive charged hadron distribution, which is
 681 comprised of roughly 60-70% pions, 15-20% kaons, and 5-15% protons. These
 682 are difficult to measure in data at the ATLAS detector, although a template sub-
 683 tractation technique has been proposed which may be effective with larger sam-
 684 ple sizes [8]. The simulation of these particles includes noticeable differences in
 685 response at low energies, which are shown in Figure 18 for FTFP_BERT. The
 686 significant differences in response between low energy protons and antiprotons
 687 are accounted for above in the definitions of E_a .

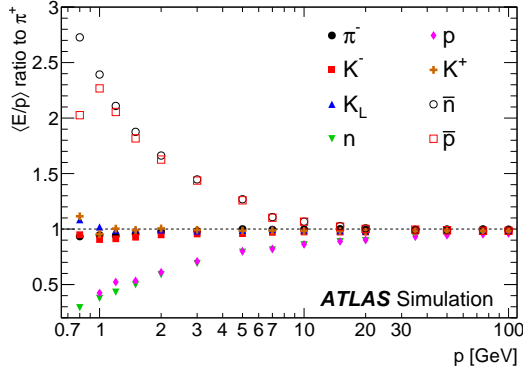


Figure 18: The ratio of the calorimeter response to single particles of various species to the calorimeter response to π^+ with the physics list FTFP_BERT.

688 8.4 SUMMARY

689 These various measurements of calorimeter response shown above for data and
 690 simulation illuminate the accuracy of the simulation of hadronic interactions at
 691 the ATLAS detector. The results were done using 2010 and 2012 data at 7 and 8
 692 TeV, but reflect the most current understanding of the detector alignment and
 693 geometry. A number of measurements focusing on a comparison between pro-
 694 tons and antiprotons suggest that FTFP_BERT models those interaction more
 695 accurately than QGSP_BERT. These measurements, among others, were the moti-

696 vation to switch the default Geant4 simulation from FTFP_BERT to QGSP_BERT
697 for all ATLAS samples.

698 Even with these updates, there are a number of small, approximately 5%, dis-
699 crepancies in response between the data and simulation at low energies. At higher
700 energies the simulation of hadronic interactions is very consistent with data.
701 Chapter 9 discusses how to use these observed differences to constrain the jet
702 energy scale and its associated uncertainties.

703

704 JET ENERGY RESPONSE AND UNCERTAINTY

705 9.1 MOTIVATION

706 As jets form a major component of many physics analyses at ATLAS, it is cru-
 707 cial to carefully calibrate the measurement of jet energies and to derive an un-
 708 certainty on that measurement. These uncertainties have often been the domi-
 709 nant systematic uncertainty in high-energy analyses at the Large Hadron Col-
 710 llider ([LHC](#)). Dijet and multijet balance techniques provide a method to constrain
 711 the [JES](#) and its uncertainty in data, and provide the default values used for ATLAS
 712 jet measurements at most energies [7]. These techniques are limited by their re-
 713 liance on measuring jets in data, so they are statistically limited in estimating
 714 the jet energy scale at the highest jet energies. This chapter presents another
 715 method for estimating the jet energy scale and its uncertainty which builds up a
 716 jet from its components and thus can be naturally extended to high jet momen-
 717 tum. Throughout this chapter the jets studied are simulated using [Pythia8](#) with
 718 the CT10 parton distribution set [27] and the AU2 tune [3], and corrections are
 719 taken from the studies including data and simulation in Chapter 8.

720 As described in Section 7.2, jets are formed from topological clusters of energy
 721 in the calorimeters using the anti- k_t algorithm. These clusters originate from a
 722 diverse spectrum of particles, in terms of both species and momentum, leading to
 723 significantly varied jet properties and response between jets of similar produced
 724 momentum. Figure 19 shows the simulated distribution of particles within jets
 725 at a few examples energies. The E/p measurements provide a thorough under-
 726 standing of the dominant particle content of jets, the charged hadrons.

727 9.2 UNCERTAINTY ESTIMATE

728 Simulated jets are not necessarily expected to correctly model the energy de-
 729 posits in the calorimeters, because of the various discrepancies discussed in Chap-
 730 ter 8. To evaluate a jet energy response, the simulated jet energies are compared
 731 to a corrected jet built up at the particle level. Each cluster in a jet is associated
 732 to the truth particle which deposited it, and the energy in that cluster is then
 733 corrected for a number of effects based on measurements in data. The primary
 734 corrections come from the single hadron response measurements in addition to
 735 response measured using the combined test beam which covers higher momen-
 736 tum particles [10]. These corrections include both a shift (Δ), in order to make the
 737 simulation match the average response in data, and an uncertainty (σ) associated
 738 with the ability to constrain the difference between data and simulation. Some of
 739 the dominant sources of uncertainty are itemized in Table ?? with typical values,
 740 and the full list considered is described in detail in the associated paper [8]. These

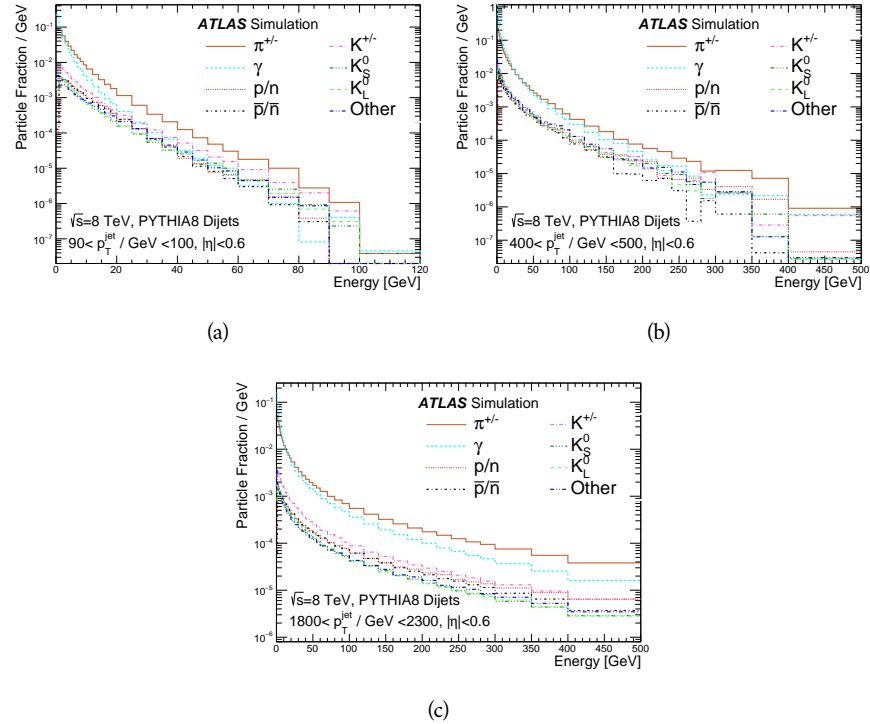


Figure 19: The spectra of true particles inside anti- k_t , $R = 0.4$ jets with (a) $90 < p_T/\text{GeV} < 100$, (b) $400 < p_T/\text{GeV} < 500$, and (c) $1800 < p_T/\text{GeV} < 2300$.

741 uncertainties cover differences between the data and simulation in the modeling
 742 of calorimeter response to a given particle. No uncertainties are added for the
 743 difference between particle composition of jets in data and simulation.

744 From these terms, the jet energy scale and uncertainty is built up from indi-
 745 vidual energy deposits in simulation. Each uncertainty term is treated indepen-
 746 dently, and are taken to be gaussian distributed. The resulting scale and uncer-
 747 tainty is shown in Figure 20, where the mean response is measured relative to
 748 the calibrated energy reported by simulation. The dominant uncertainties come
 749 from the statistical uncertainties on the E/p measurements at lower energies and
 750 the additional uncertainty for out of range measurements at higher energies. The
 751 total uncertainty from this method at intermediate jet energies is comparable to
 752 other simulation-based methods [4] and is about twice as large as in-situ meth-
 753 ods using data [7]. This method is the only one which provides an estimation
 754 above 1.8 TeV, however, and so is still a crucial technique in analyses that search
 755 for very energetic jets.

756 These techniques can also be used to measure the correlation between bins of
 757 average reconstructed jet momentum across a range of p_T and $|\eta|$, where cor-
 758 relations are expected because of a similarity in particle composition at similar
 759 energies. Figure 21 shows these correlations, where the uncertainties on jets in
 760 neighboring bins are typically between 30% and 60% correlated. The uncertainty
 761 on all jets becomes significantly correlated at high energies and larger pseudora-
 762 pidities, when the uncertainty becomes dominated by the single term reflecting
 763 out of range particles.

Abbrev.	Description	Δ (%)	σ (%)
In situ E/p	The comparison of $\langle E/p \rangle_{\text{COR}}$ as described in Chapter 8 with statistical uncertainties from 500 MeV to 20 GeV.	0-3	1-5
CTB	The main $\langle E/p \rangle$ comparison uncertainties, binned in p and $ \eta $, as derived from the combined test beam results, from 20 to 350 GeV [10].	0-3	1-5
E/p Zero Fraction	The difference in the zero-fraction between data and MC simulation from 500 MeV to 20 GeV.	5-25	1-5
E/p Threshold	The uncertainty in the EM calorimeter response from the potential mismodeling of threshold effects in topological clustering.	0	0-10
Neutral	The uncertainty in the calorimeter response to neutral hadrons based on studies of physics model variations.	0	5-10
K_L	An additional uncertainty in the response to neutral K_L in the calorimeter based on studies of physics model variations.	0	20
E/p Misalignment	The uncertainty in the p measurement from misalignment of the ID.	0	1
Hadrons, $p > 350$ GeV	A flat uncertainty for all particles above the energy range or outside the longitudinal range probed with the combined test beam.	0	10

Table 1: The dominant sources of corrections and systematic uncertainties in the [JES](#) estimation technique, including typical values for the correcting shift (Δ) and the associated uncertainty (σ).

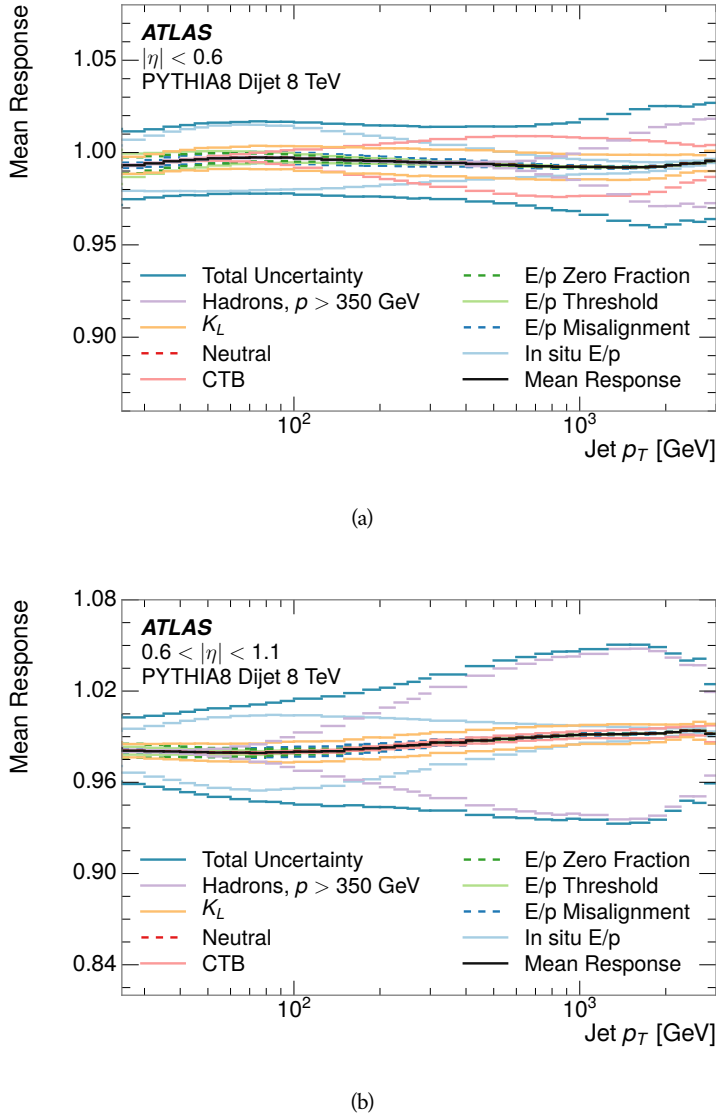


Figure 20: The `JES` uncertainty contributions, as well as the total `JES` uncertainty, as a function of jet p_T for (a) $|\eta| < 0.6$ and (b) $0.6 < |\eta| < 1.1$.

764 9.3 SUMMARY

765 The technique described above provides a jet energy scale and uncertainty by
 766 building up jet corrections from the energy deposits of constituent particles. The
 767 E/p measurements are crucial in providing corrections for the majority of parti-
 768 cles in the jets. The uncertainty derived this way is between 2 and 5% and is about
 769 twice as large at corresponding momentum than jet balance methods. However
 770 this is the only uncertainty available for very energetic jets using 2012 data and
 771 simulation, and repeating this method with Run 2 data and simulation will be
 772 important in providing an uncertainty for the most energetic jets in 13 TeV col-
 773 lisions.

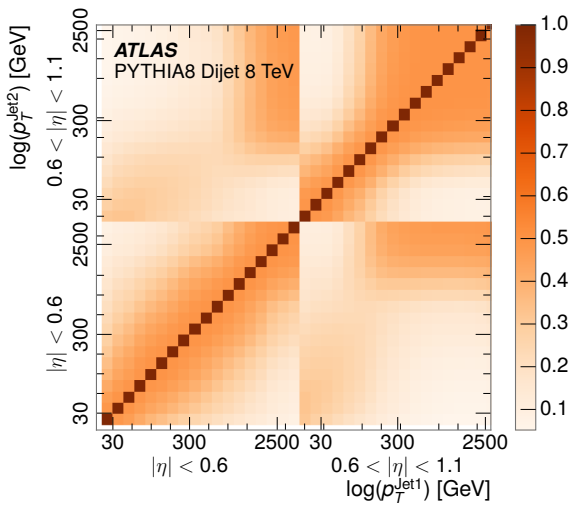


Figure 21: The JES correlations as a function of jet p_T and $|\eta|$ for jets in the central region of the detector.

774

PART V

775

SEARCH FOR LONG-LIVED PARTICLES

776

You can put some informational part preamble text here.

10

777

778 LONG-LIVED PARTICLES IN ATLAS

779 10.1 OVERVIEW AND CHARACTERISTICS

780 10.2 SIMULATION

781

782 EVENT SELECTION

783 The Long-Lived Particles ([LLPs](#)) targeted by this search differ in their interactions
 784 with the detector from [SM](#) particles primarily because of their large mass. When
 785 produced at the energies available at the [LHC](#), that large mass results in a low β
 786 and such slow-moving particles heavily ionize in detector material. Each layer
 787 of the pixel detector provides a measurement of that ionization, through time
 788 over threshold ([ToT](#)), as discussed in Section [6.3.1](#). The ionization in the pixel
 789 detector, quantified in terms of dE/dx , provides the major focus for this search
 790 technique, both for its discriminating power and also because of the large range
 791 of lifetimes where it can be used. The dE/dx variable needs to be augmented
 792 with a few additional selection requirements to form a complete search.

793 Ionization is not currently available in any form during triggering, so this
 794 search instead relies on E_T^{miss} to trigger signal events. Although triggering on
 795 E_T^{miss} is not particularly efficient, E_T^{miss} is often large for many production mech-
 796 anisms of [LLPs](#), as discussed in Section [10.1](#).

797 Ionization is most effective in rejecting backgrounds for well-measured, high-
 798 momentum tracks, so some basic requirements on quality and kinematics are
 799 placed on the particles considered in this search. In particular a newly introduced
 800 tracking variable is very effective in removing highly-ionizing backgrounds caused
 801 by overlapping tracks. A few additional requirements are placed on the tracks
 802 considered for [LLP](#) candidates that increase background rejection by targeting
 803 specific types of [SM](#) particles. These techniques provide a significant analysis
 804 improvement over previous iterations of ionization-based searches on ATLAS
 805 by providing additional background rejection with minimal loss in signal effi-
 806 ciency.

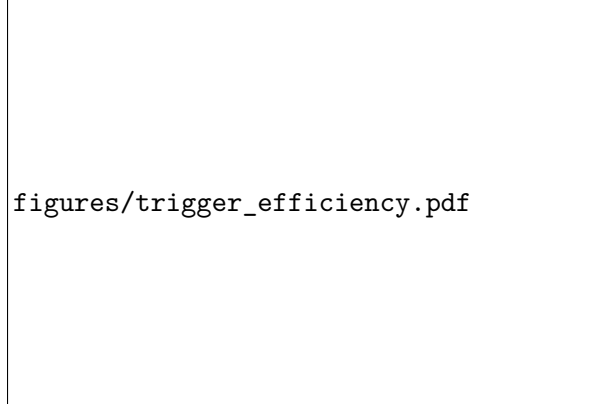
807 The ionization measurement with the Pixel detector can be calibrated to pro-
 808 vide an estimator of $\beta\gamma$. That estimate, together with the momentum measure-
 809 ment provided by tracking, can be used to reconstruct a mass for each track
 810 which traverses the pixel detector. That mass variable will be peaked at the [LLP](#)
 811 mass for any signal, and provides an additional tool to search for an excess. In
 812 addition to an explicit requirement on ionization, this search constructs a mass-
 813 window for each targeted mass range in order to evaluate any excess of events
 814 and to set limits.

815 The strategy discussed here is optimized for lifetimes of $O(1) - O(10)$ ns.
 816 Pixel ionization is especially useful in this regime as particles only need to prop-
 817 agate through the first seven layers of the inner detector, about 37 cm from the
 818 beam axis. The search is still competitive with other searches for [LLPs](#) at longer
 819 lifetimes, because the primary discriminating variables are still applicable even
 820 for particles that do not decay within the detector. Although the basic strategy
 821 remains the same for all lifetimes, two signal regions are defined to optimize
 822 separately for intermediate and long lifetime particles.

823 11.1 TRIGGER

824 Triggering remains one of the primary difficulties in defining an event selection
 825 with high signal efficiency in a search for **LLPs**. There are no triggers available in
 826 the current ATLAS system that can fire directly from a high momentum track
 827 with large ionization (Section 6.6). Although in some configurations a charged
 828 **LLP** can fire muon triggers, this requirement introduces significant model depen-
 829 dence on both the allowed lifetimes and the interactions in the calorimeter.

830 For a search targeting particles which may decay prior to reaching the muon
 831 system, the most efficient available trigger is based on missing energy. As dis-
 832 cussed in Section 10.1, signal events can produce E_T^{miss} by two primary mech-
 833 anisms. The decays of R-Hadrons to neutralinos can produce missing energy
 834 when the neutralinos go undetected in the calorimeters. **LLPs** which do not de-
 835 cay before the calorimeters also can produce missing energy because they do
 836 not deposit much energy. Either case to some extent relies on kinematic degrees
 837 of freedom to produce missing energy, as the pair-produced **LLPs** tend to bal-
 838 ance each other in the transverse plane. That balance results in a relatively low
 839 efficiency for long-lifetime particles, roughly 40%, and efficiencies between 65%
 840 and 95% for shorter lifetimes depending on both the mass and the lifetime, as
 841 seen in Figure 22.



figures/trigger_efficiency.pdf

Figure 22: The trigger efficiency of the E_T^{miss} trigger as a function of mass and lifetime.

842 11.2 KINEMATICS AND ISOLATION

843 After the trigger requirement, each event is required to have a primary vertex
 844 reconstructed from at least two well-measured tracks in the inner detector, each
 845 with $p_T > 400$ MeV. If more than one such vertex exists, the primary vertex is
 846 taken to be the one with the largest summed track momentum for all tracks as-
 847 sociated to that vertex. The offline reconstructed E_T^{miss} is required to be above
 848 130 GeV to additionally reject **SM** backgrounds. The transverse missing energy
 849 is calculated using fully reconstructed and calibrated offline objects, as described
 850 in Section 7.5. In particular the E_T^{miss} definition in this selection uses jets recon-
 851 structed with the anti- k_t algorithm with radius $R = 0.4$ from clusters of energy

852 in the calorimeter (Section 7.2) and with $p_T > 20$ GeV, as well as reconstructed
 853 muons, electrons, and tracks not identified as another object type.

854 The E_T^{miss} distributions are shown for data and a few simulated signals in Figure 23, after the trigger requirement. The cut placed at 130 GeV is 95% efficient
 855 for metastable and 90% efficient for stable particles, because of the missing en-
 856 ergy generating mechanisms discussed previously. The distribution of data in
 857 this figure and subsequent figures in this section can be interpreted as the dis-
 858 tribution of backgrounds, as any signal contamination would be negligible if
 859 present at these early stages of the selection (prior to the final requirement on
 860 mass). The background falls rapidly with missing energy, motivating the direct
 861 requirement on E_T^{miss} for the signal region. Although a higher requirement than
 862 the specified value of 130 GeV would seem to increase the search potential from
 863 these early distributions, other requirements are more optimal when taken as a
 864 whole. The specific values for each requirement in signal region were optimized
 865 considering the increase in discovery reach for tightening the requirement on
 866 each discriminating variable. **NOTE: Is it interesting to discuss the signal re-**
 867 **gion optimization process in detail? I could add another section on how**
 868 **the values were determined, although in truth it is at least partially his-**
 869 **torical precedence.**

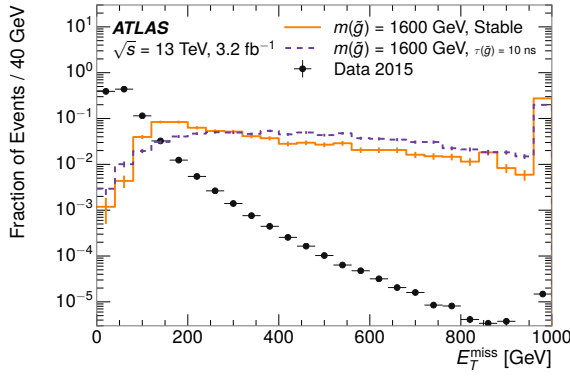


Figure 23: The distribution of E_T^{miss} for data and simulated signal events, after the trigger requirement.

871 Potential signal events are then required to have at least one candidate LLP
 872 track. Although the LLPs are produced in pairs, many models do not consistently
 873 yield two charged particles. For example, in the R-Hadron model highlighted
 874 here, only 20% of events have two charged R-Hadrons while 47% of events have
 875 just one. A signal region requiring two charged candidates could be a powerful
 876 improvement in background rejection for a larger dataset, but it is not consid-
 877 ered in this version of the analysis as it was found to be unnecessary to reject the
 878 majority of backgrounds.

879 For a track to be selected as a candidate, it must have $p_T > 50$ GeV and pass
 880 basic quality requirements. The track must be associated to the primary vertex. It
 881 must also have at least seven clusters in the silicon layers in the inner detector to
 882 ensure an accurate measurement of momentum. Those clusters must include one
 883 in the innermost layer if the extrapolated track is expected to pass through that

layer. And to ensure a reliable measurement of ionization, the track is required to have at least two clusters in the pixel detector that provide a measurement of dE/dx .

At this point in the selection, there is a significant high-ionization background from multiple tracks that significantly overlap in the inner detector. Previous version of this analysis have rejected these overlaps by an explicit overlap rejection between pairs of fully reconstructed tracks, typically by requiring no additional tracks within a cone around the candidate. This technique, however, fails to remove the background from tracks that overlap so precisely that the tracks cannot be separately resolved.

A new method, added in Run 2, identifies cluster shapes that are likely formed by multiple tracks based on a neural network classification algorithm. The number of clusters that are classified this way in the pixel detector for a given track is called N_{split} . As the shape of clusters requires significantly less spatial separation to identify overlaps than it does to reconstruct two fully resolved tracks, this variable is more effective at rejecting backgrounds from overlaps. Figure 24 shows the dependence of ionization on N_{split} ; as N_{split} increases the mean of dE/dx grows significantly up to twice the expected value when $N_{\text{split}} = 4$.

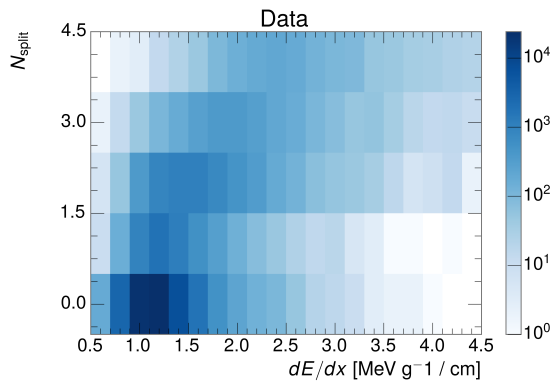


Figure 24: The dependence of dE/dx on N_{split} in data after basic track hit requirements have been applied.

This requirement is very successful in reducing the long positive tail of the dE/dx distributions, as can be seen in Figure 25. Comparing the distribution for “baseline tracks”, tracks with only the above requirements on clusters applied and before the requirement on N_{split} , to the distribution with $N_{\text{split}} = 0$, it is clear that the fraction of tracks with large dE/dx is reduced by several orders of magnitude. The isolated tracks are very close to the dE/dx distribution of identified muons, which are extremely well isolated on average. Figure 25 also includes the distribution of dE/dx in an example signal simulation to demonstrate how effective dE/dx is as a discriminating variable with this isolation applied. The background falls rapidly for $dE/dx > 1.8 \text{ MeV g}^{-1} \text{ cm}^2$ while the majority of the signal, approximately 90% depending on the mass, falls above that threshold.

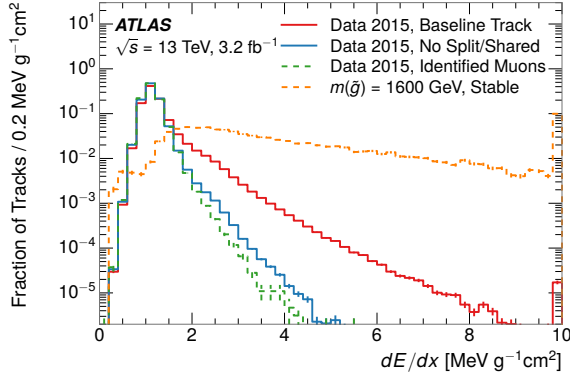


Figure 25: The distribution of dE/dx with various selections applied in data and simulated signal events.

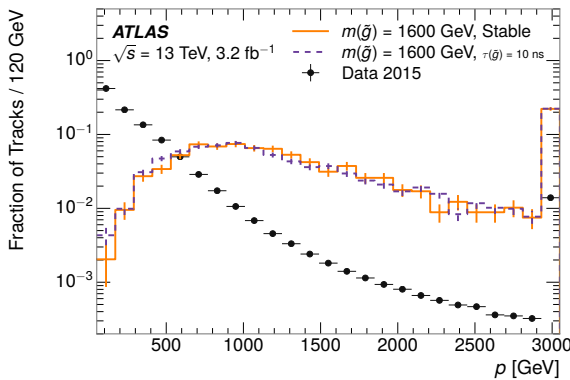


Figure 26: The distribution of track momentum for data and simulated signal events, after previous selection requirements have been applied.

913 11.3 STANDARD MODEL REJECTION

914 11.4 IONIZATION

915 11.4.1 DE/DX CALIBRATION

916 11.4.2 MASS ESTIMATION

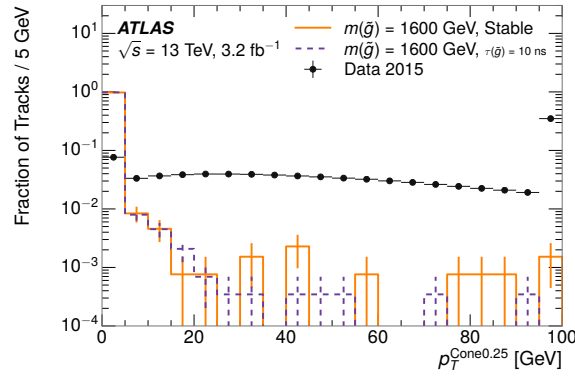


Figure 27: The distribution of summed tracked momentum within a cone of $\Delta R < 0.2$ around the candidate track for data and simulated signal events, after previous selection requirements have been applied.

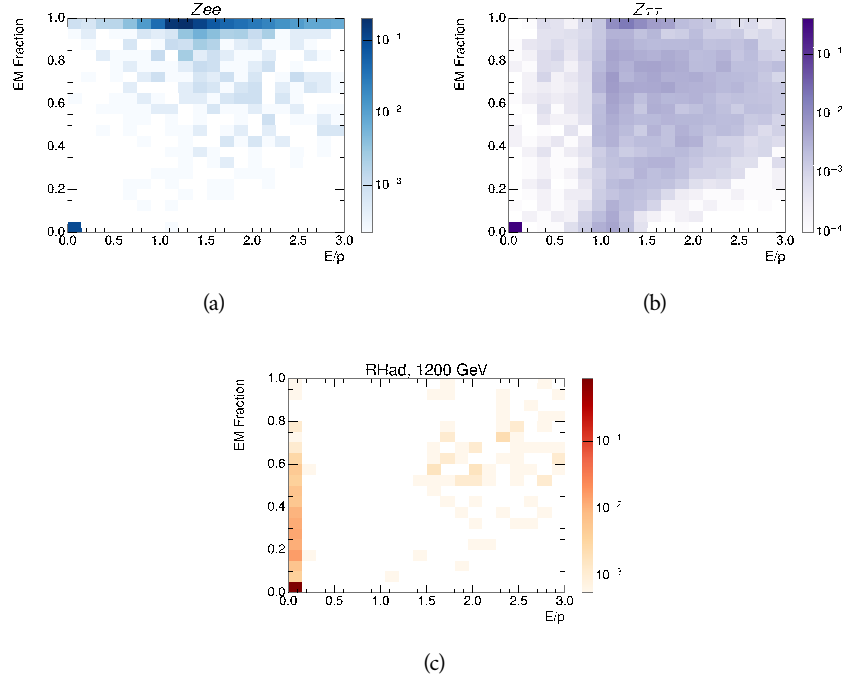


Figure 28: The normalized, two-dimensional distribution of E/p and EM fraction for simulated (a) $Z \rightarrow ee$, (b) $Z \rightarrow \tau\tau$ and (c) 1200 GeV R-Hadron events.

12

917

918 BACKGROUND ESTIMATION

919 12.1 BACKGROUND SOURCES

920 12.2 PREDICTION METHOD

921 12.3 VALIDATION AND UNCERTAINTY

13

922

923 SYSTEMATIC UNCERTAINTIES AND RESULTS

924 13.1 SYSTEMATIC UNCERTAINTIES

925 13.2 FINAL YIELDS

14

⁹²⁶

⁹²⁷ INTERPRETATION

⁹²⁸ 14.1 CROSS SECTIONAL LIMITS

⁹²⁹ 14.2 MASS LIMITS

⁹³⁰ 14.3 CONTEXT FOR LONG-LIVED SEARCHES

931

PART VI

932

CONCLUSIONS

933

You can put some informational part preamble text here.

15

934

935 SUMMARY AND OUTLOOK

936 15.1 SUMMARY

937 15.2 OUTLOOK

938

PART VII

939

APPENDIX

940

A

941

942 INELASTIC CROSS SECTION

B

943

944 APPENDIX TEST

945 Examples: *Italics*, SMALL CAPS, ALL CAPS ¹. Acronym testing: **UML!** (**UML!**) –
946 **UML! – UML! (UML!) – UML!s**

This appendix is temporary and is here to be used to check the style of the document.

947 B.1 APPENDIX SECTION TEST

948 Random text that should take up a few lines. The purpose is to see how sections
949 and subsections flow with some actual context. Without some body copy be-
950 tween each heading it can be difficult to tell if the weight of the fonts, styles,
951 and sizes use work well together.

952 B.1.1 APPENDIX SUBECTION TEST

953 Random text that should take up a few lines. The purpose is to see how sections
954 and subsections flow with some actual context. Without some body copy be-
955 tween each heading it can be difficult to tell if the weight of the fonts, styles,
956 and sizes use work well together.

957 B.2 A TABLE AND LISTING

958 Curabitur tellus magna, porttitor a, commodo a, commodo in, tortor. Donec in-
959 terdum. Praesent scelerisque. Maecenas posuere sodales odio. Vivamus metus la-
960 cus, varius quis, imperdiet quis, rhoncus a, turpis. Etiam ligula arcu, elementum a,
961 venenatis quis, sollicitudin sed, metus. Donec nunc pede, tincidunt in, venenatis
962 vitae, faucibus vel, nibh. Pellentesque wisi. Nullam malesuada. Morbi ut tellus ut
963 pede tincidunt porta. Lorem ipsum dolor sit amet, consectetur adipiscing elit.
964 Etiam congue neque id dolor.

965 There is also a Python listing below Listing 1.

1 Footnote example.

LABITUR BONORUM PRI NO	QUE VISTA	HUMAN
fastidii ea ius	germano	demonstratea
suscipit instructior	titulo	personas
quaestio philosophia	facto	demonstrated

Table 2: Autem usu id.

966 B.3 SOME FORMULAS

Due to the statistical nature of ionisation energy loss, large fluctuations can occur in the amount of energy deposited by a particle traversing an absorber element². Continuous processes such as multiple scattering and energy loss play a relevant role in the longitudinal and lateral development of electromagnetic and hadronic showers, and in the case of sampling calorimeters the measured resolution can be significantly affected by such fluctuations in their active layers. The description of ionisation fluctuations is characterised by the significance parameter κ , which is proportional to the ratio of mean energy loss to the maximum allowed energy transfer in a single collision with an atomic electron:

You might get unexpected results using math in chapter or section heads.
Consider the pdfspacing option.

$$\kappa = \frac{\xi}{E_{\max}} \quad (1)$$

E_{\max} is the maximum transferable energy in a single collision with an atomic electron.

$$E_{\max} = \frac{2m_e\beta^2\gamma^2}{1 + 2\gamma m_e/m_x + (m_e/m_x)^2},$$

967 where $\gamma = E/m_x$, E is energy and m_x the mass of the incident particle, $\beta^2 =$
968 $1 - 1/\gamma^2$ and m_e is the electron mass. ξ comes from the Rutherford scattering
969 cross section and is defined as:

$$\xi = \frac{2\pi z^2 e^4 N_{Av} Z \rho \delta x}{m_e \beta^2 c^2 A} = 153.4 \frac{z^2}{\beta^2} \frac{Z}{A} \rho \delta x \text{ keV},$$

970 where

971 z charge of the incident particle
 N_{Av} Avogadro's number
 Z atomic number of the material
 A atomic weight of the material
 ρ density
 δx thickness of the material
972 κ measures the contribution of the collisions with energy transfer close to
973 E_{\max} . For a given absorber, κ tends towards large values if δx is large and/or if
974 β is small. Likewise, κ tends towards zero if δx is small and/or if β approaches
975 1.

2 Examples taken from Walter Schmidt's great gallery:
<http://home.vrweb.de/~was/mathfonts.html>

Listing 1: A floating example (listings manual)

```
1 for i in xrange(10):
    print i, i*i, i*i*i
print "done"
```

976 The value of κ distinguishes two regimes which occur in the description of
977 ionisation fluctuations:

- 978 1. A large number of collisions involving the loss of all or most of the incident
979 particle energy during the traversal of an absorber.

980 As the total energy transfer is composed of a multitude of small energy
981 losses, we can apply the central limit theorem and describe the fluctua-
982 tions by a Gaussian distribution. This case is applicable to non-relativistic
983 particles and is described by the inequality $\kappa > 10$ (i. e., when the mean
984 energy loss in the absorber is greater than the maximum energy transfer
985 in a single collision).

- 986 2. Particles traversing thin counters and incident electrons under any condi-
987 tions.

988 The relevant inequalities and distributions are $0.01 < \kappa < 10$, Vavilov
989 distribution, and $\kappa < 0.01$, Landau distribution.

990 BIBLIOGRAPHY

- 991 [1] ATLAS Collaboration. “The ATLAS Simulation Infrastructure”. In: *Eur.*
992 *Phys. J. C* 70 (2010), p. 823. doi: [10.1140/epjc/s10052-010-1429-9](https://doi.org/10.1140/epjc/s10052-010-1429-9).
993 arXiv: [1005.4568 \[hep-ex\]](https://arxiv.org/abs/1005.4568). SOFT-2010-01.
- 994 [2] ATLAS Collaboration. “A study of the material in the ATLAS inner de-
995 tector using secondary hadronic interactions”. In: *JINST* 7 (2012), P01013.
996 doi: [10.1088/1748-0221/7/01/P01013](https://doi.org/10.1088/1748-0221/7/01/P01013). arXiv: [1110.6191 \[hep-ex\]](https://arxiv.org/abs/1110.6191).
997 PERF-2011-08.
- 998 [3] ATLAS Collaboration. *Summary of ATLAS Pythia 8 tunes*. ATL-PHYS-PUB-
999 2012-003. 2012. url: <http://cds.cern.ch/record/1474107>.
- 1000 [4] ATLAS Collaboration. “Jet energy measurement with the ATLAS detector
1001 in proton–proton collisions at $\sqrt{s} = 7$ TeV”. In: *Eur. Phys. J. C* 73 (2013),
1002 p. 2304. doi: [10.1140/epjc/s10052-013-2304-2](https://doi.org/10.1140/epjc/s10052-013-2304-2). arXiv: [1112.6426 \[hep-ex\]](https://arxiv.org/abs/1112.6426).
1003 PERF-2011-03.
- 1004 [5] ATLAS Collaboration. “Single hadron response measurement and calorime-
1005 ter jet energy scale uncertainty with the ATLAS detector at the LHC”. In:
1006 *Eur. Phys. J. C* 73 (2013), p. 2305. doi: [10.1140/epjc/s10052-013-2305-1](https://doi.org/10.1140/epjc/s10052-013-2305-1). arXiv: [1203.1302 \[hep-ex\]](https://arxiv.org/abs/1203.1302).
1007 PERF-2011-05.
- 1008 [6] ATLAS Collaboration. “Electron and photon energy calibration with the
1009 ATLAS detector using LHC Run 1 data”. In: *Eur. Phys. J. C* 74 (2014), p. 3071.
1010 doi: [10.1140/epjc/s10052-014-3071-4](https://doi.org/10.1140/epjc/s10052-014-3071-4). arXiv: [1407.5063 \[hep-ex\]](https://arxiv.org/abs/1407.5063).
1011 PERF-2013-05.
- 1012 [7] ATLAS Collaboration. “Jet energy measurement and its systematic uncer-
1013 tainty in proton–proton collisions at $\sqrt{s} = 7$ TeV with the ATLAS detec-
1014 tor”. In: *Eur. Phys. J. C* 75 (2015), p. 17. doi: [10.1140/epjc/s10052-014-3190-y](https://doi.org/10.1140/epjc/s10052-014-3190-y). arXiv: [1406.0076 \[hep-ex\]](https://arxiv.org/abs/1406.0076).
1015 PERF-2012-01.
- 1016 [8] ATLAS Collaboration. “A measurement of the calorimeter response to sin-
1017 ggle hadrons and determination of the jet energy scale uncertainty using
1018 LHC Run-1 pp -collision data with the ATLAS detector”. In: (2016). arXiv:
1019 [1607.08842 \[hep-ex\]](https://arxiv.org/abs/1607.08842).
1020 PERF-2015-05.
- 1021 [9] ATLAS Collaboration. “Topological cell clustering in the ATLAS calorime-
1022 ters and its performance in LHC Run 1”. In: (2016). arXiv: [1603.02934 \[hep-ex\]](https://arxiv.org/abs/1603.02934).
- 1023 [10] E. Abat et al. “Study of energy response and resolution of the ATLAS barrel
1024 calorimeter to hadrons of energies from 20 to 350 GeV”. In: *Nucl. Instrum.*
1025 *Meth. A* 621.1-3 (2010), pp. 134 – 150. doi: <http://dx.doi.org/10.1016/j.nima.2010.04.054>.
1026

- 1027 [11] P. Adragna et al. "Measurement of Pion and Proton Response and Lon-
 1028 gitudinal Shower Profiles up to 20 Nuclear Interaction Lengths with the
 1029 ATLAS Tile Calorimeter". In: *Nucl. Instrum. Meth. A* 615 (2010), pp. 158–
 1030 181. doi: [10.1016/j.nima.2010.01.037](https://doi.org/10.1016/j.nima.2010.01.037).
- 1031 [12] S. Agostinelli et al. "GEANT4: A simulation toolkit". In: *Nucl. Instrum. Meth.*
 1032 A 506 (2003), pp. 250–303. doi: [10.1016/S0168-9002\(03\)01368-8](https://doi.org/10.1016/S0168-9002(03)01368-8).
- 1033 [13] N. S. Amelin et al. "Transverse flow and collectivity in ultrarelativistic
 1034 heavy-ion collisions". In: *Phys. Rev. Lett.* 67 (1991), p. 1523. doi: [10.1103/PhysRevLett.67.1523](https://doi.org/10.1103/PhysRevLett.67.1523).
- 1035 [14] N. S. Amelin et al. "Collectivity in ultrarelativistic heavy ion collisions". In:
 1036 *Nucl. Phys. A* 544 (1992), p. 463. doi: [10.1016/0375-9474\(92\)90598-E](https://doi.org/10.1016/0375-9474(92)90598-E).
- 1037 [15] B. Andersson, A. Tai, and B.-H. Sa. "Final state interactions in the (nuclear)
 1038 FRITIOF string interaction scenario". In: *Z. Phys. C* 70 (1996), pp. 499–
 1039 506. doi: [10.1007/s002880050127](https://doi.org/10.1007/s002880050127).
- 1040 [16] B. Andersson et al. "A model for low-pT hadronic reactions with general-
 1041 izations to hadron-nucleus and nucleus-nucleus collisions". In: *Nucl. Phys.*
 1042 B 281 (1987), p. 289. doi: [10.1016/0550-3213\(87\)90257-4](https://doi.org/10.1016/0550-3213(87)90257-4).
- 1043 [17] H. W. Bertini and P. Guthrie. "News item results from medium-energy
 1044 intranuclear-cascade calculation". In: *Nucl. Instr. and Meth. A* 169 (1971),
 1045 p. 670. doi: [10.1016/0375-9474\(71\)90710-X](https://doi.org/10.1016/0375-9474(71)90710-X).
- 1046 [18] L. V. Bravin et al. "Scaling violation of transverse flow in heavy ion col-
 1047 lisions at AGS energies". In: *Phys. Lett. B* 344 (1995), p. 49. doi: [10.1016/0370-2693\(94\)01560-Y](https://doi.org/10.1016/0370-2693(94)01560-Y).
- 1048 [19] L. V. Bravina et al. "Fluid dynamics and Quark Gluon string model - What
 1049 we can expect for Au+Au collisions at 11.6 AGeV/c". In: *Nucl. Phys. A* 566
 1050 (1994), p. 461. doi: [10.1016/0375-9474\(94\)90669-6](https://doi.org/10.1016/0375-9474(94)90669-6).
- 1051 [20] CMS Collaboration. "The CMS barrel calorimeter response to particle
 1052 beams from 2 to 350 GeV/c". In: *Eur. Phys. J. C* 60.3 (2009). doi: [10.1140/epjc/s10052-009-0959-5](https://doi.org/10.1140/epjc/s10052-009-0959-5).
- 1053 [21] H. S. Fesefeldt. *GHEISHA program*. Pitha-85-02, Aachen. 1985.
- 1054 [22] G. Folger and J.P. Wellisch. "String parton models in Geant4". In: (2003).
 1055 arXiv: [nucl-th/0306007](https://arxiv.org/abs/nucl-th/0306007).
- 1056 [23] B. Ganhuyag and V. Uzhinsky. "Modified FRITIOF code: Negative charged
 1057 particle production in high energy nucleus nucleus interactions". In: *Czech.
 1058 J. Phys.* 47 (1997), pp. 913–918. doi: [10.1023/A:1021296114786](https://doi.org/10.1023/A:1021296114786).
- 1059 [24] M. P. Guthrie, R. G. Alsmiller, and H. W. Bertini. "Calculation of the cap-
 1060 ture of negative pions in light elements and comparison with experiments
 1061 pertaining to cancer radiotherapy". In: *Nucl. Instrum. Meth.* 66 (1968), pp. 29–
 1062 36. doi: [10.1016/0029-554X\(68\)90054-2](https://doi.org/10.1016/0029-554X(68)90054-2).
- 1063 [25] J. Beringer et al. (Particle Data Group). "Review of Particle Physics". In:
 1064 *Chin. Phys. C* 38 (2014), p. 090001. URL: <http://pdg.lbl.gov>.

- 1069 [26] V.A. Karmanov. "Light Front Wave Function of Relativistic Composite
1070 System in Explicitly Solvable Model". In: *Nucl. Phys. B* 166 (1980), p. 378.
1071 doi: [10.1016/0550-3213\(80\)90204-7](https://doi.org/10.1016/0550-3213(80)90204-7).
- 1072 [27] Hung-Liang Lai, Marco Guzzi, Joey Huston, Zhao Li, Pavel M. Nadolsky,
1073 et al. "New parton distributions for collider physics". In: *Phys. Rev. D* 82
1074 (2010), p. 074024. doi: [10.1103/PhysRevD.82.074024](https://doi.org/10.1103/PhysRevD.82.074024). arXiv: [1007.2241 \[hep-ph\]](https://arxiv.org/abs/1007.2241).
- 1076 [28] A.D. Martin, W.J. Stirling, R.S. Thorne, and G. Watt. "Parton distributions
1077 for the LHC". In: *Eur. Phys. J. C* 63 (2009). Figures from the [MSTW Website](#),
1078 pp. 189–285. doi: [10.1140/epjc/s10052-009-1072-5](https://doi.org/10.1140/epjc/s10052-009-1072-5). arXiv: [0901.0002](https://arxiv.org/abs/0901.0002).
- 1080 [29] B. Nilsson-Almqvist and E. Stenlund. "Interactions Between Hadrons and
1081 Nuclei: The Lund Monte Carlo, Fritiof Version 1.6". In: *Comput. Phys. Com-*
1082 *mun.* 43 (1987), p. 387. doi: [10.1016/0010-4655\(87\)90056-7](https://doi.org/10.1016/0010-4655(87)90056-7).
- 1083 [30] A. Ribon et al. *Status of Geant4 hadronic physics for the simulation of LHC*
1084 *experiments at the start of LHC physics program*. CERN-LCGAPP-2010-02.
1085 2010. URL: <http://lcgapp.cern.ch/project/docs/noteStatusHadronic2010.pdf>.
- 1087 [31] A. Sherstnev and R.S. Thorne. "Parton Distributions for LO Generators".
1088 In: *Eur. Phys. J. C* 55 (2008), pp. 553–575. doi: [10.1140/epjc/s10052-008-0610-x](https://doi.org/10.1140/epjc/s10052-008-0610-x). arXiv: [0711.2473](https://arxiv.org/abs/0711.2473).
- 1090 [32] T. Sjöstrand, S. Mrenna, and P. Skands. "A Brief Introduction to PYTHIA
1091 8.1". In: *Comput. Phys. Commun.* 178 (2008), pp. 852–867. doi: [10.1016/j.cpc.2008.01.036](https://doi.org/10.1016/j.cpc.2008.01.036). arXiv: [0710.3820](https://arxiv.org/abs/0710.3820).
- 1093 [33] Peter Speckmayer. "Energy Measurement of Hadrons with the CERN AT-
1094 LAS Calorimeter". Presented on 18 Jun 2008. PhD thesis. Vienna: Vienna,
1095 Tech. U., 2008. URL: <http://cds.cern.ch/record/1112036>.

1096 DECLARATION

1097 Put your declaration here.

1098 *Berkeley, CA, September 2016*

1099

Bradley Axen

1100

1101 COLOPHON

1102

Not sure that this is necessary.